The inorganic carbon cycle of the Red Sea

Elsheikh Bashir Ali

Thesis for the degree of philosophiae doctor (PhD)
at the University of Bergen

2017

Date of defence: 14.11.2017

Year: 2017

Title: The inorganic carbon cycle of the Red Sea

Author: Elsheikh Bashir Ali

Print: AiT Bjerch AS / University of Bergen

Acknowledgements

First, I would like to express my deep gratitude to my supervisors Ingunn Skjelvan, Abdirahman M. Omar, and Truls Johannessen for giving me the opportunity to do a PhD under their guidance. Thank you all for patient supervision, enthusiasm, encouragement, continues support, all the time you have spent on my thesis, and for always keeping your doors open whenever I needed you. I would not have been able to finish my PhD without your support.

A very special thank goes to Knut Barthel for his valuable advices, patient guidance, and continues support especially in MATLAB issues.

I would like to express my heartfelt thanks to James Churchill for spending time with me and for his great effort in sharing invaluable expertise on the physical oceanography of the Red Sea.

Also, I am very grateful to all my co-authors for their contribution to my research and for sharing their expertise with me, especially Are Olsen, Elfatih Eltaib, and Salma Elageed.

Many thanks to Solveig Kringstad and Kristin Jackson for their great efforts in analyzing the carbon samples.

A very special thank you goes to Tor de Lange for his huge effort during deployment and retrieval of the mooring.

I am also grateful to Prof. Abdel Gadir D. El Hag and Prof. Mohamad E.A. Hamza (former directors of IMR) and Dr. Mudather Senebary (director of IMR) for their support, and to the IMR staff for making the time series collection and mooring mission possible. Specially, I would like to thank Srag Osman, Elfatih Eltaib , Almogeira Osman, Mostafa Mohammed, Mohammed Alamin, Abd Almonem, Ahmed Alkarory, Abd Almohsin, Yassir Hassan, Waleed Omer, and Bashir Hydar. My continues prayers for Omer Hassan, Salah Omer, and Mohammed Noor, who died in a traffic accident on their way to do sampling. I will never forget you.

I am grateful to the General Manager of the Sudanese Sea Port Corporation, the head of marine operation department, and the captain and crew of the tugboat used for deployment and retrieval of the mooring. Thanks all of them for making that mission possible. I am also grateful to the Sudanese Marine Security Department for making their boats available for the time series collection cruises.

I would like to express my deepest gratitude to all who supported me during my studies in Norway; all the people at Geophysical Institute, my friends in Bergen, my neighbors in Fantoft, and all my Sudanese friends living in Bergen.

Special thanks to my best friend Paul Bachem and Danka for all time spent together in chatting about the history, civilization and culture of the nation, and archeology.

I would like to thank the Norwegian State Educational Loan Fund and Geophysical Institute for granting me a scholarship throughout my PhD program. Thanks also for the Michelsen Centre for Research for funding the mooring and attached instrumentation based Innovation in Measurements Science and Technology (MIMT) in Bergen.

Last but not least, I would like to thank my family for their love, encouragement and prayers.

Abstract

The aim of this thesis has been to improve the general scientific understanding of the marine inorganic carbon cycle of the Red Sea. The region houses an exceptional range of ecosystems and it is considered the most important repository of biodiversity in the world with vast calcification areas rich in coral reefs. Therefore, it is important to understand the interaction between biogeochemical processes and the Red Sea ecosystem. In spite of this fact, the area is poorly studied, and this is particularly true for the marine inorganic carbon cycle.

Prior to this work, no systematic sampling of biogeochemical variables had been done off the coast of Sudan. As part of this work, a new biogeochemical time series from the Sudanese coastal waters has been established, which represents the very first data on hydrography and inorganic carbon from this part of the Red Sea. The sampling site has been operated since 2007, and here is presented data over a period of 8 years, from 2007 to 2015. Consequently, there now exists a comprehensive dataset allowing the quantification of interannual to seasonal variations in biogeochemical variables, and identify important processes that control these changes. The establishment of such a baseline is important to compare future changes caused by climate and environmental changes when approaching the high CO_2 world.

The three papers in this thesis improve and renew our understanding of the Red Sea hydrography, the inorganic carbon cycle, how the variation goes, and what drives the observed changes.

A common assumption has been that the temperature and salinity variations in the Red Sea is solely a function of local heat and mass flux. However, results from the current work evidence that advection of temperature and salinity gradients also plays a role for establishing the temperature and salinity maxima in the area (**Paper I**). The finding of this paper also show that the annual temperature range is approximately 6°C, with

highest temperatures during summer and autumn. Changes in salinity lag that of temperature with about 3 months.

The inorganic carbonate measurements (**Paper II**) document for the very first time the seasonal as well as interannual variability of dissolved inorganic carbon (DIC) and total alkalinity (A_T) in this part of the ocean. This pristine dataset has been used to construct a baseline for the inorganic carbon cycle and constitutes an important reference for years to come. Higher A_T and DIC is measured during winter compared to the summer with an annual change of approximately 40 μmol kg^{-1} for A_T and 32 μmol kg^{-1} for DIC. A_T is mainly driven by physical processes such as advection and local evaporation (through salinity changes) as well as calcification, while changes in DIC are mainly a result of air-sea exchange and likely biological activity, and to a smaller degree along shore advection.

The Red Sea, which is situated in the sub-tropical and tropical area, has previously been regarded as a net annual source for atmospheric CO_2, but this view has to be revised. **Paper III** shows that pCO_2 is high during summer and autumn and low during spring and winter, with a seasonal amplitude of about 60 μatm. Consequently, the Sudanese coastal area acts as a source for atmospheric CO_2 during summer and autumn, while during winter and spring, the area is a sink for atmospheric CO_2. Over an annual cycle, the area is a net sink of atmospheric CO_2 of size 24.4 mmol CO_2 m^{-2} y^{-1}. The change from being a net annual source for atmospheric CO_2 to becoming a net sink likely occurred in the 2000s.

List of publications

Paper I

Ali, E. B., J. H. Churchill, K. Barthel, I. Skjelvan, A. M. Omar, T. E. de Lange, and E. B. A. Eltaib, 2017. Seasonal and interannual variations of hydrographic parameters in the Sudanese coast of the Red Sea, 2009-2015, *submitted to Regional Studies in Marine Sciences journal*.

Paper II

Ali, E. B., A. M. Omar, I. Skjelvan, and T. Johannessen, 2017. Dissolved inorganic carbon and total alkalinity at the Sudanese coastal Red Sea, 2009-2013, *submitted to Regional Studies in Marine Sciences journal.*

Paper III

Ali, E. B., I. Skjelvan, A. M. Omar, A. Olsen, T. E. de Lange, T. Johannessen, S. Elageed, 2017, Sea surface pCO_2 variability and air sea gas exchange in the coastal Sudanese Red Sea, *Manuscript in preparation*.

Contents

1. Aim of the study

The main goal of this thesis has been to achieve a better understanding of the inorganic carbon cycle at the western Red Sea through unravelling the biogeochemical setting and examining the spatiotemporal variation of hydrography and carbon parameters. The environmental settings for the Red Sea is extreme in terms of biogeochemistry. The sea is considered an important calcification area with numerous coral reefs and thus its coastline is very vulnerable, but despite of this fact, there is a limited amount of scientific surveys in the area, which has resulted in a poorly understanding of the marine inorganic carbon cycle, in particular. The lack of data hinders adequate analyses of the interactions between the biogeochemical processes and the inorganic carbon cycle in the area. This is critical in light with the ongoing global warming, exemplified in a temperature increase in the Red Sea of 0.7 °C from 1985 to 2007 (Raitsos et al., 2011), expanding oxygen–minimum zones in the tropical regions (Stramma et al., 2008), and the increasing atmospheric CO_2 (Le Quéré et al., 2016).

With help of a pristine time series of hydrography and inorganic carbon data, the aim is to develop new and improved knowledge regarding the inorganic carbon cycle in this area.

2. The marine carbon system

2.1 Introduction

Due to the carbon emissions produced by the combustion of fossil fuels, production of cement, and land-use change, the atmospheric carbon dioxide (CO_2) concentration has increased exponentially from approximately 277 parts per million (ppm) at the beginning of industrial revolution in 1750 to 402 ppm in 2016. According to Le Quéré et al. (2016), combustion of fossil fuels globally emitted an amount of 9.3 ± 0.5 GtC y^{-1} into the atmosphere while land-use change contributed 1.0 ± 0.5 GtC y^{-1} during the period between 2006 and 2015. Ocean takes up about a quarter of the annual carbon emissions (2.6 ± 0.5 GtC y^{-1}) and the global residual terrestrial CO_2 sink is 3.1 ± 0.9 GtC y^{-1}. The growth rate of atmospheric CO_2 concentration for the same period is 4.5 ± 0.1 GtC y^{-1} (Le Quéré et al., 2016) (see Fig.2.1).

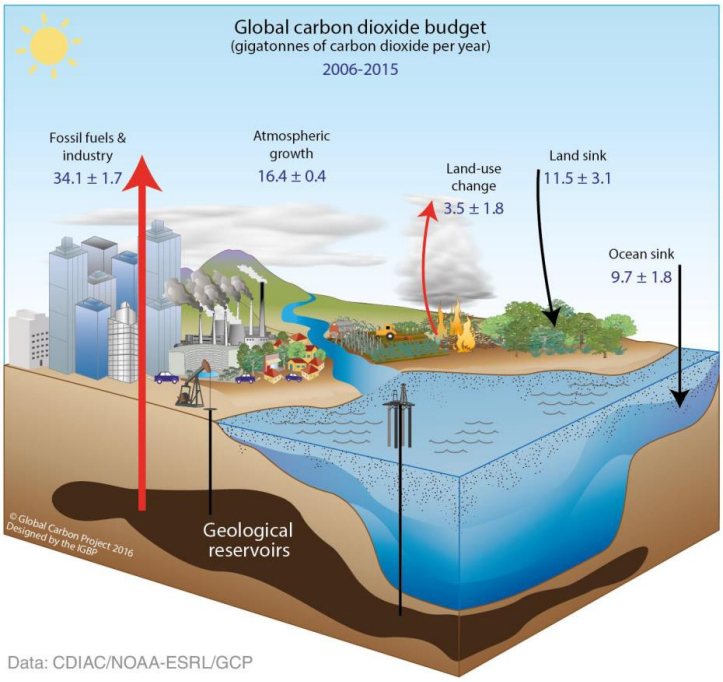

Fig. 2.1 The global carbon dioxide budget with reservoirs (in GtC y^{-1}) for the period between 2006 and 2015. 1 GtC equals 10^{15} g C. Figure from Le Quéré et al. (2016).

The CO_2 continuously cycles between the atmosphere, land, and ocean, but the amount of CO_2 is not evenly distributed, and e.g. the ocean stores about 50 times more CO_2 than the atmosphere (Field and Raupach, 2004; Zeebe and Wolf-Gladrow, 2001). The CO_2 exchange between the surface ocean and atmosphere is faster than the exchange between the surface layer and deep layer of the ocean. The latter one takes from several hundreds to thousands of years because it is driven by slower processes such as deep-water formation and the marine biological production (Emerson and Hedges, 2008).

2.2 The carbon chemistry

When CO_2 is dissolved in seawater, it is converted to aqueous CO_2 and aqueous carbonic acid (H_2CO_3). This weak acid is dissociated in two steps producing one proton (H^+) and bicarbonate ion (HCO_3^-) in the first step and two protons and carbonate (CO_3^{2-}) ion in the second step (see Eq. 2.1):

$$\underset{}{CO_2 + H_2O} \overset{K_0}{\longleftrightarrow} \underset{}{H_2CO_3^*} \overset{K_1}{\longleftrightarrow} \underset{}{H^+ + HCO_3^-} \overset{K_2}{\longleftrightarrow} \underset{}{2H^+ + CO_3^{2-}} \qquad (2.1)$$

where K_0 is Henry's constant for CO_2, and K_1 and K_2 are the first and the second dissociation constants of carbonic acid. All constants depend on temperature, salinity, and pressure of seawater (Lueker et al., 2000; Mehrbach et al., 1973). The star (*) indicate aquatic solution. Additional CO_2 dissolved in seawater generates more H^+ ions which drive more CO_3^{2-} to react with H^+ and produce HCO_3^-; known as the buffer reaction:

$$CO_2 + CO_3^{2-} + H_2O \longleftrightarrow 2HCO_3^- \qquad (2.2)$$

CO_3^{2-} is also used to form calcium carbonate ($CaCO_3$), which is a building block for skeleton and shells of some marine organisms. The $CaCO_3$ saturation state describes if the water is supersaturated or under saturated with respect to CO_3^{2-}.

The marine carbon system is described by four carbon variables; total dissolved inorganic carbon (DIC), total alkalinity (A_T), pH, and fugacity of carbon (fCO_2). If two of the carbon variables are known in addition to the equilibrium constants, the other two variables can be calculated. The total dissolved inorganic carbon (DIC), sometimes called TCO_2, C_T, or $\sum CO_2$, is defined as the sum of inorganic carbon components (Dickson and Goyet, 1994):

$$DIC = [CO_2]^* + [HCO_3^-] + [CO_3^{2-}] \tag{2.3}$$

where $[CO_2]^*$ is the sum of aquatic CO_2 and H_2CO_3.

The A_T is defined by Dickson (1981) as "the number of moles of hydrogen ion equivalent to the excess of proton acceptors over proton donors in one kilogram of sample":

$$\begin{aligned} A_T = {} & [HCO_3^-] + 2[CO_3^{2-}] + [B(OH)_4^-] + [OH^-] + [HPO_4^{2-}] + 2[PO_4^{3-}] + \\ & [H_3SiO_4^-] + [NH_3] + [HS^-] - [H^+]_F - [HSO_4^-] - [HF] - [H_3PO_4] \end{aligned} \tag{2.4}$$

where $[H^+]_F$ is the free concentration of H^+ ions. The major parts of total alkalinity in seawater is:

$$A_T = [HCO_3^-] + 2[CO_3^{2-}] + [B(OH)_4^-] + [OH^-] - [H^+]_F \tag{2.5}$$

The thermodynamic state of the acid-base system is described by the pH, which is defined as the negative logarithm of hydrogen ions concentration in gram atoms per liter:

$$pH = -\log[H^+] \tag{2.6}$$

The ocean can be considered as a natural buffer system and seawater at normal conditions is slightly basic (≈ 8.1) (Zeebe, 2012). At this pH, HCO_3^- is the major component of DIC (88.6%) followed by CO_3^{2-} (10.9%) while $[CO_2]^*$ only takes about 0.5% (Fig. 2.2).

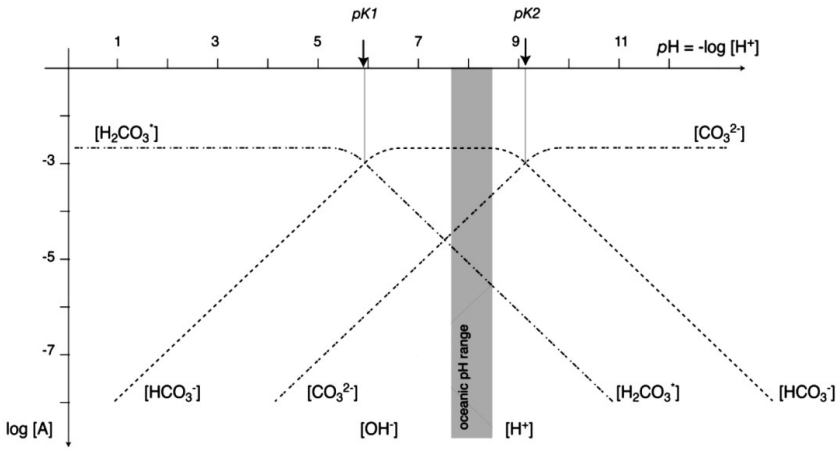

Fig. 2.2 Concentrations of the different inorganic carbon components as a function of pH. The dissociation constants of Eq. 2.1 are presented in the figure. $[H_2CO_3]^*$ equals $[CO_2]^*$, which is mentioned in the text. Figure from Sarmiento and Gruber (2006).

The partial pressure of CO_2 (pCO_2) is describing the amount of CO_2 in gas phase that is in equilibrium with seawater. According to Sarmiento and Gruber (2006), Eq. 2.1 and its dissociation constants can be reformulated to express the pCO_2 as:

$$pCO_2 = \frac{K_2}{K_0 . K_1} \frac{[HCO_3^-]^2}{[CO_3^{-2}]} \tag{2.7}$$

The fugacity of CO_2 (fCO_2) differs from pCO_2 by taking into account the non-ideal behavior of CO_2 and the difference between them is less than 0.5% (Dickson and Goyet, 1994). Zeebe and Wolf-Gladrow (2001) has described the relation between pCO_2 and fCO_2 as:

$$fCO_2 = pCO_2 \exp(P\frac{B + 2\delta}{RT}) \tag{2.8}$$

where P is the total atmospheric pressure, B is the first virial coefficient of CO_2, δ is the cross virial coefficient, R is the gas constant, and T is absolute temperature. The unit for these parameters are: fCO_2 and pCO_2 in μatm, P in Pa (1 atm =101325 Pa), B and δ are in $m^3\ mol^{-1}$, R = 8.314 J $K^{-1}mol^{-1}$, and T in Kelvin. According to Weiss (1974), B and δ can be determined, respectively, as:

$$B = (-1636.75 + 12.0408T - 3.27957 \cdot 10^{-2} T^2 + 3.16528 \cdot 10^{-5} T^3)10^{-6} \quad (2.9)$$

$$\delta = (57.7 - 0.118T)10^{-6} \quad (2.10)$$

The buffer capacity reflects the capacity of seawater to buffer changes in pH occurring because CO_2 is absorbed in the sea, and it can be quantified through the Revelle factor (γ). γ describes how fCO_2 changes for a given change in DIC when A_T is constant:

$$\gamma = \frac{\Delta fCO_2}{\Delta DIC} \frac{DIC}{fCO_2} \quad (2.11)$$

According to Takahashi et al. (1993), the Revelle factor is high (approximately 14) in cold polar and subpolar surface water and low (ca. 8) in warm surface water in tropical and subtropical areas. A global Revelle factor of 10 indicates that 1% change in DIC will drive the surface fCO_2 to change by about 10%. The current γ values are higher by one unit compared to the values prior to the industrial revolution (Sabine et al., 2004). Increasing surface fCO_2 drives the γ values to increase, thus the surface ocean has become less able to absorb additional CO_2.

2.3 The main processes controlling the marine carbon cycle

In general, the processes described below have been assessed and make up the theoretical basis in the general carbon cycle for the three papers presented in this thesis.

2.3.1 Solubility pump

The solubility of any gas in seawater depends on temperature and salinity (Gordon and Jones, 1973). Therefore, cold water at high latitudes contain more CO_2 in equilibrium with the atmosphere than warm water at lower latitudes. By help of the global thermohaline circulation (Broecker, 1991), dissolved CO_2 sinks towards deep layers through deep-water formation at high latitudes, while at low latitudes, upwelling brings carbon rich deep water to the surface, which is warm and has low gas solubility, and thus, CO_2 is emitted into the atmosphere. This physical process (called solubility pump) takes long time (hundreds of years) and constantly exchange CO_2 between ocean and atmosphere.

2.3.2 Biological pump

The biological pump can be split into two parts: organic carbon pump and calcium carbonate counter pump.

The organic carbon pump is described through the primary production taking place in the surface water and remineralization of organic matter which occurs in sub-surface and deep waters. During primary production, the phytoplankton use aquatic CO_2 from the surface water and transform it into organic matter through photosynthesis:

$$106CO_2 + 122H_2O + 16HNO_3 + H_3PO_4 \xrightarrow{sunlight} (CH_2O)_{106}(NH_3)_{16}H_3PO_4 + 138O_2 \quad (2.12)$$

A minor part of the sinking organic particles is trapped in the sediment, while most of the organic matter is remineralized by bacteria and regenerated into CO_2 and nutrients. Upwelling of deep water brings water rich in carbon and nutrients into the surface (Fig. 2.3).

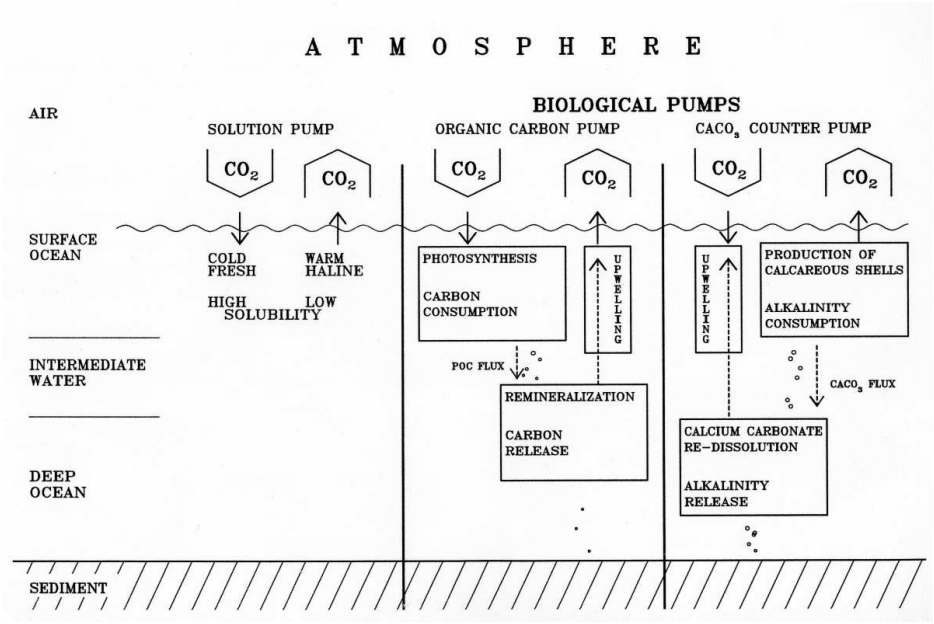

Fig. 2.3 The solubility and biological CO_2 pumps in the ocean (Heinze et al., 1991*).*

The calcium carbonate counter pump is described through the production of calcium carbonate in the surface layer and dissolution in the deep waters. The coral reefs and many planktonic organisms such as Coccolithophorids uses $CaCO_3$ to form their shells and skeletons according to

$$Ca^{2+} + 2HCO_3^- \rightarrow CaCO_3 + CO_2 + H_2O \qquad (2.13)$$

In the deep water, where the conditions are more acidic, the $CaCO_3$ shells are dissolved:

$$H^+ + CaCO_3 \rightarrow Ca^{2+}(aq) + CO_3^{2-}(aq) + H^+ \rightarrow HCO_3^- \qquad (2.14)$$

Photosynthesis will decrease DIC, and fCO_2, while pH increases. A_T is only affected to a minor degree, by a small increase due to nutrient consumption (Fig.2.4). On the other hand, calcium carbonate formation decreases A_T by two units and DIC by one

unit, and only to a minor degree decreases pH and increases fCO_2 (Fig.2.4) (Zeebe and Wolf-Gladrow, 2001).

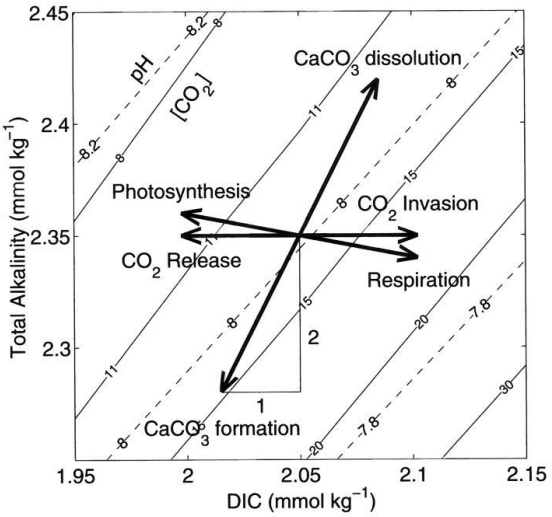

Fig. 2.4 Effects of the different processes on DIC, A_T, pH, and [CO_2] (from Zeebe and Wolf-Gladrow, 2001).

2.3.3 Air-sea gas exchange

Air-sea gas exchange affects the DIC and pH (Fig. 2.4), and the direction of CO_2 fluxes between air and sea depends on differences in CO_2 concentration (fCO_2 or pCO_2) between atmosphere and surface ocean, as well as the wind at sea surface, the temperature and to a small degree the salinity. The CO_2 flux is determined as

$$F = SK(fCO_2^{seawater} - fCO_2^{atmosphere}) \tag{2.15}$$

where S is solubility of CO_2 in seawater (mol kg^{-1}atm^{-1}), which depends on temperature and salinity of the surface water (Weiss, 1974). K is the gas transfer velocity, which depends on the molecular diffusivity, kinematic viscosity, and turbulence at the air-

water interface. K is commonly parameterized as a function of wind speed because the wind speed is important for the turbulence.

There are numerous relationships of K in the literature (Liss and Merlivat, 1986; Wanninkhof, 1992; Wanninkhof and McGillis, 1999; Nightingale et al., 2000; Sweeney et al., 2007), and in this thesis, the one from Nightingale et al. (2000) is used:

$$K = \left(0.222U_{10}^2 + 0.333U_{10}\right)\left(\frac{Sc}{660}\right)^{-1/2} \tag{2.16}$$

where U_{10} is wind speed at 10 m above the sea surface, and Sc is the Schmidt number, which show the ratio between kinematic viscosity and molecular diffusivity.

3. Description of the study area

The Red Sea separates the northeastern Africa from the Arabian Peninsula, and linking between the tropical and sub-tropical parts of the ocean. It is about 1930 km long, on average 200 km wide, and represent an area of approximately 0.46 x 10^6 km^2. The Red Sea is connected with the Gulf of Aden and the Indian Ocean through the narrow strait of Bab Al Mandab (BAM) (Fig. 3.1). In the northern part, the Red Sea is divided into two main branches; Gulf of Aqaba and Gulf of Suez, the latter is linked with the Mediterranean Sea via the Suez Canal. The bottom topography of the Red Sea is naturally wedge shaped with relatively large maximum depth (2920 m) in the central of the basin. The average depth of Bab Al Mandab strait is about 300 m while the Gulf of Suez has a relatively flat bottom with depth about 60 m. The Gulf of Aqaba is a deep basin with narrow shelves and a mean depression depth of about 1200 m (Morcos, 1970; Patzert, 1974; Edwards, 1987; Maillard and Soliman, 1986).

The climate of the Red Sea is influenced by two wind regimes (Fig. 3.1). North of 19° N the north-northwesterly wind (NNW), which is controlled by eastern Mediterranean weather systems, is active throughout the year. During the summer, the NNW wind extends as far south as the BAM Strait. The area south of 14°N is influenced by Indian Monsoon system, which switches between south-southeasterly wind (SSE) during winter and NNW during summer. The area between 14°N and 19°N is characterized as a convergent zone for the wind field for most of the year, see Fig. 3.1 (Morcos, 1970; Pedgley, 1974; Patzert, 1974).

The average sea surface temperature of the Red Sea is about 26°C in the north and 30°C in the south during summer, while during winter, the temperature is 2-4°C lower. The highest surface temperatures (28°C - 34°C) are found in the south-central parts of the Red Sea where the wind field is convergent and thus weak for most of the year (Sofianos and Johns, 2003). Because of high evaporation, low precipitation, and supply of relative fresh water from the south, the surface salinity of the Red Sea is increasing from approximately 36.5 psu in the south to more than 41.0 psu in the north. Deeper

than about 300 m, the temperature is about 21.5°C and salinity about 40.5 psu all the way to the bottom (Edwards, 1987).

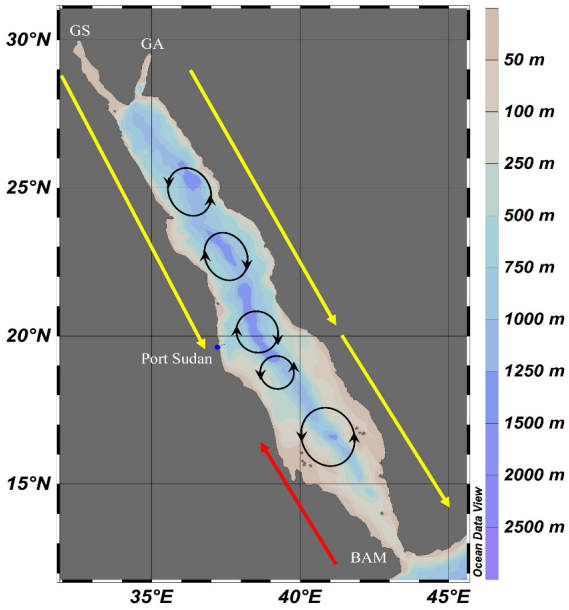

Fig. 3.1 Map showing the location and bathymetry of the Red Sea. Bab Al Mandab Strait (BAM), Gulf of Suez (GS), and Gulf of Aqaba (GA) are indicated in the figure. Arrows refer to wind directions: NNW wind = yellow arrows; SSE wind = red arrows. Arrows to the right in the figure indicate summer situation, while those to the left are winter situation. Locations of cyclonic and anticyclonic gyres are also indicated.

There are four dominant water masses in the Red Sea, all affected by two major masses in the Gulf of Aden. During wintertime, the Gulf of Aden Surface Water (GASW) enters the Red Sea through the BAM Strait as a result of southeasterly winds (Morcos, 1970; Pedgley, 1974; Patzert, 1974; Quadfasel and Baudner, 1993). At deeper layers, the Red Sea Overflow Water (RSOW), which is a mixture of Red Sea Intermediate Water (RSIW) and Red Sea Deep Water (RSDW), is observed to flow out of the Red Sea throughout the year (Sofianos and Johns, 2003; Yao et al., 2014 a; b). During

summer, when northwesterly winds extend as far south as the BAM Strait, an outflow of Red Sea Surface Water (RSSW) is induced while south of the BAM Strait, southwesterly winds provoke an upwelling of Gulf of Aden Intermediate Water (GAIW), as it moves towards the Red Sea (Morcos, 1970; Patzert, 1974; Smeed, 1997).

The overall circulation of the Red Sea is influenced by the monsoon winds. Surface currents during winter flow from the Indian Ocean northwards throughout the Red Sea while the direction of currents during summer, is reversed i.e. flowing southwards to the Indian Ocean as deep currents. The surface circulation in the south (around 15°N) is featured by anticylonic rotation during winter and cyclonic rotation during summer. Serval cyclonic and anticyclonic gyres are distributed along the north-south axis of the Red Sea, and the strength, size and location of these gyres vary with time (Fig.3.1) (Morcos and Soliman, 1974; Quadfasel and Bauner, 1993; Yao et al., 2014 a; b).

4. Objectives

The main objective of this thesis is to explore the inorganic carbon cycle of the Red Sea, which is poorly known with respect to seasonal and interannual variability. The main objectives has been to:

-establish and maintain a time series to document seasonal and interannual changes.

-understand the coastal physical oceanographic setting.

-determine the drivers of biogeochemical variability at multiple time scales.

The thesis is divided into three topics, which are covered in separate papers. The three papers are based upon the new time series of discrete and continuous data collected in the Sudanese coastal waters off Port Sudan during the period 2007-2015.

Generally, there are few studies focusing on temporal variations of temperature or salinity within the Red Sea, and more specific, there is no study, which fully has dealt with the dynamics responsible for the observed temperature and salinity variations. **Paper I** aims towards getting a better understanding on the temporal variability of ocean physics based on temperature and salinity as well as pointing at the mechanisms responsible for these variations. **Paper II** aims to unravel the seasonality of the marine inorganic carbon cycle, represented by DIC and A_T, the relationship with the hydrography, and the drivers causing the observed variability of DIC and A_T.

Paper III focus on how to determine the air-sea flux of CO_2 over an annual cycle using continuous atmospheric and oceanic pCO_2 measurements of moored autonomous sensors deployed in our study area. Further, the seasonal variations and drivers of the oceanic pCO_2 variability have been identified.

5. Summary

Combined, the three papers in this thesis improve and renew our understanding of the Red Sea inorganic carbon cycle, the hydrography, how it varies, and what drives the observed changes.

A new time-series of discrete and continuous data from the Sudanese coast shows that, in contradiction to previous knowledge, advection in addition to local heat and mass flux drive the temperature and salinity variability (**Paper I**). The surface temperature (SST) is at the highest value during summer and autumn and at lowest during winter, with a seasonal amplitude of approximately 6°C. The salinity lagged temperature with about 3 months, and the seasonal amplitude was about 1.1 psu. Validated satellite-derived SST data confirmed the above temperature findings, which was also confirmed by computed T arrived from the local heat flux when taking into account the adjustment for advection and mixing. The impact of alongshore advection on seasonal distribution of temperature and salinity has been estimated using a simple model based on gradient features of temperature, salinity and geostrophic surface velocity. The geostrophic surface velocity is computed from sea level anomaly field. SSS increases from south to north and the maximum SST zone is located south of the area of study, in the central Red Sea. The geostrophic current directs form south to north during spring and summer introducing relatively warm and fresh water from the south. During autumn and winter, the geostrophic current reverses and brings waters, which is cold and more saline towards the study area. The close match between estimated and observed seasonal temperature and salinity supports the conclusion that the observed seasonal T and S signals off Port Sudan are largely the product of local heat and mass flux and alongshore advection.

A study of the seasonal variations of A_T and DIC off the Sudanese coast (**Paper II**) shows that A_T and DIC are high during winter and low during summer with an average annual variability of 40 $\mu mol\,kg^{-1}$ for A_T and 32 $\mu mol\,kg^{-1}$ for DIC. The seasonal signals are associated with the maxima and minima of salinity described in **Paper I.** Advection of water, and thus changing salinity is an important factor controlling A_T variations,

while the observed change in DIC is primarily controlled by air-sea gas exchange, through change in temperature, and, very likely, by biological production. The remaining changes of DIC are caused by alongshore advection during autumn and winter (**Paper I**). Seasonality for DIC and A_T have been reconstructed using the observed DIC-SST and A_T-SSS relationships together with SST satellite data and SSS-advection from **Paper I.** The calculated results fit the observed variability of DIC and A_T. The interannual change of the surface A_T were twice as high as the seasonal variation whereas for surface DIC, the interannual changes were found to be less than the seasonal changes.

An annual cycle of oceanic pCO_2 between October 2014 and October 2015 is presented in **Paper III**. The highest values occur during summer-autumn and lowest during winter-spring, with a seasonal amplitude of approximately 60 µatm overlaid a high frequency signal of about 10 µatm. More than half of the variability of oceanic pCO_2 is driven by SST changes, which is in line with findings in **Paper II** that half of the observed change in DIC is due to temperature driven air-sea CO_2 exchange. The pCO_2-SST relationship throughout a year has an elliptical shape, which confirms that beside the temperature influence, other processes also contribute in controlling pCO_2 changes, e.g. along-coast advection described in **Paper I**. Based on oceanic pCO_2 and atmospheric data, the area is a net annual sink for atmospheric CO_2 of size 24.4 mmol CO_2 m^{-2} y^{-1}. During summer and autumn, the area act as a source for atmospheric CO_2, while during winter and spring the area is a sink for atmospheric CO_2. The air-sea gas exchange was examined for the period between 1977-2015. It shows that the area most likely switched from being a net annual source area for atmospheric CO_2 to becoming a net annual sink during the 2000s.

Most of the work done is pristine and for this reason important, and a useful baseline is made for a region with extreme condition in term of physical, chemical, and ecological properties. Through this baseline, future changes in climate and environment and their predicted trends and impacts can be documented and assessed. In this regard, sustaining the coastal time series initiated by this study will be of extreme importance.

6. Future plans

In light of the vulnerable environment of the Red Sea as well as its natural extreme environmental settings, there are several topics, which are important and interesting to explore in the future. Multiple stressors, e.g. increasing temperature, deoxygenation, and rising atmospheric CO_2 concentration, affect the ocean and its ecosystems. Warming of the ocean will e.g. decrease the gas solubility, and thus, reduce oceanic oxygen concentration, which has been observed at several locations (Shepherd et al., 2017, and references therein). However, the current understanding and implications of such a deoxygenation is not yet resolved.

Further, exploration of precipitation and dissolution of calcium carbonate, $CaCO_3$, has not been sufficiently discussed in this thesis due to lack of time and data scarceness. The Red Sea is a region with high $CaCO_3$ production, and recent studies by Takahashi et al. (2014), Steiner et al. (2014), and Elageed et al. ("Oxygen and alkalinity utilization rates in the Red Sea", manuscript in preparation) show that such a production affects A_T through calcification within the pelagic layer and by corals.

At present, ocean acidification is not an imminent threat for the Red Sea. The area is super saturated with respect to calcium carbonate, and thus has relatively high resistance to Ocean Acidification (Elageed, 2010; Omer, 2010). However, this might change in the future, and continuous monitoring of the marine carbon cycle is important.

7. Bibliography

Broecker, W.S., 1991. The Great Ocean Conveyor. Oceanography, 4, 79-89.

Dickson, A. G., 1981. An exact definition of total alkalinity and a procedure for the estimation of alkalinity and total inorganic carbon from titration data, Deep-Sea Res., 28A:609-623.

Dickson, A., Goyet, C., 1994. Handbook of methods for the analysis of the various parameters of the carbon dioxide system in sea water, ORNL/CDIAC-74.

Edwards, F.J., 1987. Climate and oceanography, in: Edwards, A. J., Head, S. M. (Eds), Red Sea, Pergamon press, Oxford, pp. 45-70.

Elageed, S., 2010. Factors controlling the total alkalinity in the Arabian Sea and Red Sea, MS thesis, Univ. of Bergen, Bergen, Norway.

Emerson, S., Hedges, J., 2008. Chemical Oceanography and the Marine Carbon Cycle, 462 pp., Cambridge University Press, Cambridge.

Field C. B., Raupach, M. R. (Eds), 2004. The Global Carbon Cycle: Integrating Humans, Climate, and the Natural World. Island Press, Washington, DC.

Gordon, L., Jones, L., 1973. The effect of temperature on carbon dioxide partial pressures in seawater, Marine Chemistry, 1 (4), 317-322.

Heinze, C., Maier-Reimer, E., Winn, K., 1991. Glacial pCO2 reduction by the World Ocean - experiments with the Hamburg Carbon Cycle Model, Paleoceanography, 6, 395-430.

Le Quéré, **C.,** Andrew, R. M., Canadell, J. G., Sitch, S., Korsbakken, J. I., Peters, G. P., Manning, A. C., Boden, T. A., Tans, P. P., Houghton, R. A., Keeling, R. F., Alin, S., Andrews, O. D., Anthoni, P., Barbero, L., Bopp, L., Chevallier, F., Chini, L.P., Ciais. P., Currie, K., Delire, C., Doney, S. C., Friedlingstein, P., Gkritzalis, T., Harris, I., Hauck, J., Haverd, V., Hoppema, M., Klein Goldewijk, K., Jain, A.K., Kato, E., Körtzinger, A., Landschützer, P., Lefêvre, N., Lenton, A., Lienert, S., Lombardozzi, D., Melton, J. R., Metzl, N., Millero, F., Monteiro, P.M.S., Munro, D.R., Nabel, J. E. M. N., Nakaoka, S.-i., O'Brien, K, Olsen, A., Omar, A. M., Ono, T., Pierrot, D., Poulter, B., Rödenbeck, C., Salisbury, J.E., Schuster, U., Schwinger, J., Séférian, R., Skjelvan, I., Stocker, B. D., Sutton, A.J., Takahashi, T., Tian, H., Tilbrook, B., van der Laan-Luijks, I. T., van der Werf, G.R., Viovy, N., Walker, A. P., Wiltshire, A.J., Zaehle, S., **2016.** Global carbon budget 2016, Earth Syst. Sci. Data, 8, 605–649,

Liss, P. S., Merlivat, L., 1986. Air- Sea gas exchange rates: introduction and synthesis .In: The

Role of Air-Sea Exchange in Geochemical Cycling, (ed .P.Buat-Menard).NATO ASI Series C: Mathematical and Physical Science 185,D.Reidel Publishing Company .pp.113-127 .

Lueker, T.J., Dickson, A. G., Keeling. C. D., 2000. Ocean pCO2 calculated from dissolved inorganic carbon, alkalinity, and equations for K1 and K2: validation based on laboratory measurements of CO2 in gas and seawater at equilibrium. Mar. Chem. 70: 105– 119.

Maillard, C., Soliman, G., 1986. Hydrography of the Red Sea and exchanges with the Gulf of Aden in summer. Oceanologica Acta, 9 - N°3, 249–269.

Mehrbach, C., Culberson, C. H., Hawley, J. E., Pytkowicz, R. M., 1973. Measurement of the apparent dissociation constants of carbonic acid in seawater at atmospheric pressure. Limnology and Oceanography 18:897-907.

Morcos, S.A., 1970. Physical and chemical oceanography of the Red Sea, Oceanography and Marine Biology Annual Review, 8**,** 73-202.

Morcos, S., Soliman, G.F., 1974. Circulation and deep water formation in the Northern Red Sea in winter (Based on R/V Mabahisss sections, January–February, 1935). In L'Océanographie physique de la Mer Rouge, pp. 91–103, Centre National pour l'Exploration des Océans (CNEXO), Paris, 91–103.

Nightingale, P.D., Malin, G., Law, C. S., Watson, A. J., Liss, P. S., Liddicoat, M. I., Boutin, J., Upstill-Goddard, R. C., 2000. In-situ evaluation of air-sea gas exchange parameterizations using novel conservative and volatile tracers, Global Biogeochem. Cycles, 14, 373-387.

Omer, W. M. M., 2010. Ocean acidification in the Arabian Sea and the Red Sea - factors controlling pH MS thesis, Univ. of Bergen, Bergen, Norway.

Patzert, W. C., 1974. Wind-induced reversal in Red Sea circulation, Deep Sea Res., 21, 109–121.

Pedgley, D. E., 1974. An outline of the weather and climate of the Red Sea, in L'Oceanographie Physique de la Mer Rouge, pp. 9 – 27, Cent. Natl. pour l'Exploitation des Oceans, Paris.

Quadfasel, D., Baudner, H., 1993. Gyre-scale circulation cells in the Red Sea, Oceanol. Acta, 16, 221-229.

Raitsos, D. E., Hoteit, I., Prihartato, P. K., Chronis, T., Triantafyllou, G., Abualnaja, Y., 2011. Abrupt warming of the Red Sea, Geophys. Res. Lett., 38, L14601, doi: 10.1029/2011GL047984.

Sabine, C.L., Feely, R., Gruber, N., Key, R., Lee, K., Bullister, J., Wanninkhof, R., Wong, C. S., . Wallace, D. W, Tilbrook, B. Millero, F. J., Peng, T., Kozyr, A., Ono, T., Rios, A., 2004. The oceanic sink for anthropogenic CO_2, Science 305, 367-371.

Sarmiento, J. L., Gruber, N., 2006. Ocean Biogeochemical Dynamics. Princeton University Press, Princeton, NJ, USA.

Shepherd, J.G., Brewer, P.G., Oschlies, A. Watson, A. J., 2017. Ocean ventilation and deoxygenation in a warming world: introduction and overview, Phil. Trans. R. Soc A 375: 20170240, http://dx.doi.org/10.1098/rsta.2017.0240.

Smeed, D. A., 1997. Seasonal Variation of the flow in the strait of Bab el Mandab, Oceanologica Acta, 20 - N°6, 773–781.

Sofianos, S. S., Johns, W. E., 2003. An Oceanic General Circulation Model (OGCM) investigation of the Red Sea circulation: 2. Three-dimensional circulation in the Red Sea, J. Geophys. Res., 108, NO. C3, 3066, doi:10.1029/2001JC001185.

Steiner, Z., Erez, J., Shemesh, A., Yam, R., Lazar, B., 2014. Basin-scale estimates of pelagic and coral reef calcification in the Red Sea and Western Indian Ocean, PANS, Vol. 111, No. 46, 16303-16308.

Stramma, L., Johnson, G.C., Sprintall, J., and Mohrholz, V., 2008. Expanding Oxygen-Minimun Zones in the Tropical Oceans, Science, 320.

Sweeney, C., Gloor, E., Jacobson, A. R., Key, R. M., McKinley, G., Sarmiento, J. L., Wanninkhof, R., 2007. Constraining global air-sea gas exchange for CO2 with recent bomb 14C measurements, Global Biogeochem. Cycles, 21, GB2015, doi:10.1029/ 2006GB002784.

Takahashi, T., Olafsson, J., Goddard, J., Chipman, D.W., Sutherland, S.C., 1993. Seasonal variation of CO2 and nutrients in the high-latitude surface oceans: A comparative study. Glob. Biogeochem. Cycles 7, 843–878.

Takahashi, T., Sutherland, S. C., Chipman, D. W., Goddard, J. G., Ho, C., Newberger, T., and others. 2014. Climatological distributions of pH, pCO2, total alkalinity, and $CaCO_3$ saturation in the global surface ocean, and temporal changes at selected locations. Mar. Chem. 164:95–125.

Wanninkhof, R., 1992. Relationship between gas exchange and wind speed over the ocean, J. Geophys. Res., 97, 7373-7381.

Wanninkhof, R., McGillis, W. M., 1999. A cubic relationship between gas transfer and wind speed, Geophys. Res. Lett., 26, 1889-1893.

Weiss, R. F., 1974. Carbon dioxide in water and sea water: the solubility of a non -ideal gas, Mar. Chem., 2:203-215.

Yao, F. C., Hoteit, I., Pratt, L. J., Bower, A. S., Zhai, P., Kohl , A., Gopalakrishnan, G., 2014a. Seasonal overturning circulation in the Red Sea: 1. Model validation and summer circulation. Journal of Geophysical Research-Oceans. 119:2238-2262.

Yao, F., Hoteit, I., Pratt, L. J., Bower, A. S., Kohl, A., Gopalakrishnan, G., Rivas, D., 2014b. Seasonal overturning circulation in the Red Sea: 2. Winter circulation, J. Geophys. Res. Oceans, 119, 2263–2289, doi:10.1002/ 2013JC009331.

Zeebe, R.E., Wolf-Gladrow, D., 2001. CO2 in Seawater: Equilibrium, Kinetics, Isotopes, Elsevier Oceanography Series: 2001.

Zeebe, R. E., 2012. History of seawater carbonate chemistry, atmospheric CO2, and ocean acidification, Annu. Rev. Earth Planet. Sci., 40(1).

I

Paper I

Seasonal and interannual variations of hydrographic parameters in the Sudanese coast of the Red Sea, 2009-2015

Ali, E. B., J. H. Churchill, K. Barthel, I. Skjelvan, A. M. Omar, T. E. de Lange, and E. B. A. Eltaib

Submitted to Regional Studies in Marine Sciences journal

Seasonal and interannual variations of hydrographic parameters in the Sudanese coast of the Red Sea, 2009-2015

Elsheikh B. Ali[1, 2], James H. Churchill[3], Knut Barthel[1], Ingunn Skjelvan[4, 1], Abdirahman M. Omar[4, 1], Tor E. de Lange[1], and Elfatih B. A. Eltaib[2]

[1]Geophysical Institute (GFI), University of Bergen (UiB), Bergen, Norway
[2]Institute of Marine Research (IMR), Red Sea University (RSU), Port Sudan, Sudan
[3]Department of Physical Oceanography, Woods Hole Oceanographic Institution, Woods Hole, Massachusetts 02543, USA
[4]Uni Research Climate, Bergen, Norway

Abstract:

The temporal variations of temperature and salinity in the Sudanese coast of the Red Sea have been studied based on new time series acquired over 2009-2015 from a mooring and from survey cruises. The observations show that temporal variations in temperature and salinity above the main pycnocline are dominated by seasonal signals. Highest temperature of approximately 32°C occur during summer and early autumn and lowest temperature of roughly 26°C are seen in winter. The seasonal salinity signal lags that of temperature by roughly 3 months, and varies from approximately 38.5 psu in late spring and early summer to 39-40 psu in late autumn and early winter. Using estimates of heat flux, circulation and horizontal temperature/salinity gradients derived from a number of sources, we determined that the observed seasonal temperature and salinity could not be the product of local heat and mass flux alone, but also due to advection of alongshore temperature and salinity gradients.

Keywords

Coastal Red Sea; temperature; salinity; time series; seasonality; alongshore advection

1. Introduction

Encompassing a highly diverse ecosystem, the Red Sea ranks as one of the warmest and most saline of the world's seas. Fluctuations in near-surface temperature and salinity within Red Sea coastal waters can have profound ecological consequences, particularly for the numerous reef systems that fringe the Red Sea basin. It is well established that the growth rate and overall health

of coral communities are highly sensitive to changes in temperature and affected to a lesser degree by variations in salinity (e.g., Ferrier-Pages et al., 1999; Furby et al., 2013; Kuanui et al., 2015). It is also well established that changes in temperature and salinity affect the inorganic carbon cycle; e.g. warmer water reduces the gas solubility and thus increases the flux of carbon dioxide from the surface water into the atmosphere, and changes in alkalinity are tightly connected to changes in salinity (e.g. Sarmiento and Gruber, 2006, and references therein).

There are currently few published studies of the temporal variations of temperature or salinity within the Red Sea. Churchill et al. (2014) examined temperature fluctuations waters of the coastal zone of the central Red Sea off the Saudi Arabian coast using data acquired from moorings deployed at ~50 m depth. They showed that near-surface (upper 15 m) temperature variations span a range of order 8ºC and are predominately due to a seasonal signal with a range of order 6ºC. A seasonal near-surface temperature signal with a similar range was reported by Sultan and Ahmad (1991) based on sea surface measurements acquired off of Jeddah Saudi Arabia, by Berman et al. (2003) based on hydrographic data acquired in summer and winter, and by Davis et al. (2011) based on temperature sensors placed on platform reef tops. Published reports of temporal salinity variations in the Red Sea are very rare. Churchill et al. (2014) briefly discussed salinity records from the moorings references above but showed no time series. Sultan and Ahmad (1991) presented an 8-year record of monthly-averaged surface salinities acquired off of Jeddah Saudi Arabia that span a range of order 1 psu, but noted that the salinities may have been affected by discharge from the Jeddah desalinization facility.

It is notable that all of the studies reviewed above utilized data from the coastal zone of the central Red Sea west of the Saudi Arabian coast and so may not be representative of temperature and salinity variations over the full Red Sea. Furthermore, no study has dealt fully with the dynamics responsible for the observed temperature and salinity variations. While some studies have related temperature variations to surface heat flux (Sultan and Ahmad, 1991; Berman et al., 2003; Churchill et al., 2014), the manner in which temperature and salinity variations are influenced by water mass transport has not yet been assessed.

The work reported here is aimed at furthering the understanding of temperature and salinity variations in the coastal Red Sea. Using data from moored instruments and hydrographic surveys, we describe the temporal variations in temperature and salinity within near-surface coastal waters off of Port Sudan, Sudan (Fig. 1). With the aid of reanalysis and satellite-derived

data, we examine the mechanisms responsible for these variations, concentrating on the relative importance of local processes (surface heat and mass flux) and water mass advection. Our focus is on the seasonal signal of temperature and salinity. As noted above, previous observations have shown that the range of near-surface temperature variation in the central Red Sea is primarily due to the seasonal signal.

In the following sections, we first describe the data sets and methodology employed (Section 2). We then detail the temperature and salinity variations in the coastal zone off of Port Sudan (Section 3.1) and examine the dominant mechanisms responsible for these variations (Section 3.2). We conclude with a summary of our findings and a discussion of how they relate to prior work on the dynamics of the Red Sea system (Section 4).

2. Data and Methods

Our analysis employed six datasets. Three were used to describe the seasonal variation of temperature, salinity and potential density (σ_θ) off of Port Sudan, and three were employed in assessing the mechanisms responsible for the seasonal variation of these properties. Below, we detail these data sets and present our methods for estimating near-surface temperature and salinity change.

2.1 Measurements of coastal temperature and salinity

2.1.1 Cruise data

Our study employed cruise measurements of temperature and salinity acquired at two set of stations (Fig. 1): near-shore stations in the area of Port Sudan Harbour (PSH), and stations situated along a transect between Port Sudan and the Sanganeb atoll reef (30 km northeast of Port Sudan) (the SPS stations). The data acquired at all stations were from a SAIV A/S model 204 CTD, deployed using a hand winch and equipped with an inductive cell conductivity sensor (resolution 0.01 mS cm^{-1}, accuracy ± 0.02 mS cm^{-1}), a temperature sensor (resolution 0.001, accuracy ± 0.01°C), and a pressure sensor (resolution 0.01 mbar, accuracy ± 0.02%).

The salinity was computed to a resolution of 0.01 psu and to an accuracy of ± 0.02 psu (Operating Manual for SAIV CTD model 204, 2006). Calibration of the salinity measurements was done using water samples acquired during a subset of the CTD casts by a Hydrobios 2-liter

water sampler. The bottle salinity was determined using the Guildline Portasal Salinometer (model 8410A) to an accuracy of ± 0.003 psu (Datasheet for Guildline 8410A Portasal, 2002).

Measurements at the PSH stations encompassed the period of 2010-2013 and extended vertically from near the surface to roughly 150 m depth. Measurements from the SPS transect were from 2009-2013 and vertically extended to roughly 200 m. Both sets of data resolved the seasonal signal of temperature and salinity (Fig. 2). The SPS data were taken at a quarterly interval (collected roughly during October, February, April, and July), whereas the PSH data interval was shorter but varied considerably.

2.1.2 Mooring data

Additional temperature and salinity time series data of our study were acquired from a Sea Bird CTD (SBE 37-SM MICROCAT, SN 3939) affixed to a mooring deployed on 1 October 2014 at station 4 (37.395°E, 19.720°N; Fig. 1) of SPS transect. The bottom depth at the mooring location was ~800 m, and the CTD, which was positioned at a nominal depth of 37 m, was set to record at hourly intervals. The mooring was recovered on 15 October 2015. The CTD was equipped with conductivity (resolution 0.0001, accuracy ± 0.003 mS cm^{-1}), temperature (resolution 0.0001, accuracy ± 0.002°C), and pressure (resolution 0.002%, accuracy ± 0.1%) sensors. The salinity measurements were calibrated using bottle salinity measurements determined as described above.

2.1.3 Satellite-derived sea surface temperature

The sea surface temperature (SST) data used in this study were from the NOAA High-resolution Blended Analysis of Daily SST (Version 2) dataset. Formulated by combining observations from different platforms (satellites, ships, buoys) (Reynolds et al., 2007), the dataset is comprised of daily temperatures specified on a 0.25° latitude by 0.25° longitude global grid.

2.2 Data used to compute heat and salt fluxes

2.2.1 The Simple Ocean Data Assimilation (SODA) dataset

The SODA dataset is comprised of data produced by an ocean general circulation model with an average resolution of 0.25° latitude by 0.4° longitude, and 40 vertical levels. Direct contemporaneous observations are continuously used to correct the model error of the generated ocean variables (Carton et. al., 2008). We employed SODA data to estimate horizontal salinity

and temperature gradients, which were used in the computation of heat and salt fluxes due to horizontal advection.

2.2.2 NCEP datasets

We extracted data from the National Centers for Environmental Prediction (NCEP) / National Center for Atmospheric Research (NCAR) dataset to estimate the surface wind stress as well as surface heat and mass flux in our study region. All data were from a 2° latitude by 2° longitude cell centered at 37.50°E, 20.00°N. The wind stress was computed from 10 m NCEP Reanalysis-2 wind velocities according to the formulae of Large and Pond (1981).

To compute the surface heat flux, we downloaded individual surface heat flux components: net shortwave radiation (Q_{sw}), net longwave radiation (Q_{lw}), latent heat flux (Q_l) and sensible heat flux (Q_s). Net surface heat flux (Q_{net}) was determined according to (Wallcraft et al., 2008):

$$Q_{net} = Q_{sw} - Q_{lw} + Q_l + Q_s \quad (1)$$

Net surface mass flux (m s^{-1}) was computed as:

$$M = E - P \quad (2)$$

where E is the evaporation rate and P is the precipitation rate. P was computed from the NCEP Reanalysis-2 precipitation rate (P_R, kg m^{-2} s^{-1}) according to:

$$P = \frac{P_R}{\rho_0} \quad (3)$$

where ρ_0 is the fresh water density. E was computed from the latent heat flux according to (Sumner and Belaineh, 2005):

$$E = \frac{-Q_l}{\rho_0 \lambda} \quad (4)$$

where λ is latent heat of vaporization of water (2.3×10^6 J kg^{-1}).

To assess the NCEP heat flux estimates, we compared the net heat flux series determined using measurement from an air–sea interaction buoy maintained in the central Red Sea (at 38° 30.1′E; 22° 9.6′N) over 2008-2010 (Farrar et al., 2009; Bower and Farrar, 2015) with a net heat flux time series determined from NCEP data for the cell which included the buoy location. The two series

were highly correlated (R^2=0.89) and exhibited closely matched seasonal cycles, with net heat flux into the ocean over March through September and net heat loss over the rest of the year. The net heat transfer over the two years of the comparison (2009-2010) was negative for both series, but was slightly larger in magnitude for the buoy-derived series (-1.2 x 10^9 versus -0.9 x 10^9 J m^{-2}).

2.2.3 Sea Level Anomaly (SLA)

Estimation of near-surface velocities was done using altimeter-derived sea level anomaly (SLA) fields computed with respect to the CLS01 (Centre de Localisation des Satellites) long-term mean sea surface height. Downloaded from AVISO (http://www.aviso.oceanobs.com/), the SLA fields were determined by combining sea level data from all available satellites and objectively mapping SLA on a 0.25° latitude by 0.25° longitude grid. We computed geostrophic surface velocity from the gridded SLA field through:

$$u_G = -\frac{g}{f}\frac{\partial \delta}{\partial y}\,;\, v_G = \frac{g}{f}\frac{\partial \delta}{\partial x} \qquad (5)$$

where δ is SLA, u_G and v_G are the east and north components of geostrophic velocity, respectively, g is the gravitational acceleration and f is local Coriolis parameter.

2.3 Estimation of near-surface temperature and salinity changes

With the data described above, we sought to roughly assess the contributions of surface heat and mass fluxes and horizontal advection in driving the observed seasonal signal of near-surface temperature and salinity in our study region. We did not consider the effects of mixing or vertical advection as these were not well suited for study with the available data. Our focus was on temperature and salinity changes in the layer above the permanent pycnocline. For simplicity, we assumed that this layer extended to a constant depth, h. We also assumed that the advective changes in temperature and salinity were principally due to fluxes in the alongshore (roughly N-S in the area of Port Sudan) direction. With these assumptions, the changes in temperature (T) and salinity (S) averaged over the surface layer may be approximated as:

$$\frac{\partial T}{\partial t} = \frac{Q_{net}}{h\rho_s C_p} - V\frac{\partial T}{\partial y} \qquad (6)$$

$$\frac{\partial S}{\partial t} = \frac{M}{h} S - V \frac{\partial S}{\partial y} \quad (7)$$

where C_p is the specific heat capacity of water (4.2×10^3 J kg^{-1}), y is the alongshore coordinate, ρ_s is the near-surface density and V is the vertically-averaged alongshore velocity in the layer above the main pycnocline.

Our approach was to determine the near-surface temperature and salinity signal from observed starting values of T_o and S_0, respectively. For simplicity, we took the horizontal temperature and salinity gradients as constants (determined from the SODA data as explained in Section 2.2). With these assumptions, the seasonal temperature and salinity signals were estimated from

$$T(t) = T_0 + \int_0^t \left[\frac{Q_{net}(\tau)}{h \rho_s C_p} - V(\tau) \frac{\partial T}{\partial y} \right] d\tau \quad (8)$$

$$S(t) = S_0 + \int_0^t \left[\frac{M(\tau)}{h} S(\tau) - V(\tau) \frac{\partial S}{\partial y} \right] d\tau. \quad (9)$$

3. Results

3.1 Seasonal variation

3.1.1 SPS and PSH

The measurements from the coastal hydrographic surveys (SPS and PSH) clearly show a seasonal signal in near-surface values of temperature, salinity and σ_θ (Fig. 2). The near-surface temperature signal is marked by maxima of close to 32°C during summer and early autumn and minima of roughly 26°C in winter. The timing and range of this signal closely match those of the seasonal temperature signal shown by Churchill et al. (2014) based on moored measurements acquired in the coastal zone of the central Red Sea. In particular, Churchill et al. (2014) show highest near-surface temperatures, of roughly 32°C, over July-October contrasting with the lowest near-surface temperatures, of roughly 26°C, over January-March (their Fig. 2). The seasonal near-surface salinity signal lags the temperature signal by roughly 3 months with maxima (39.0-39.5 psu at SPS and 39-40 psu at PSH) in late autumn/early winter and minima (approximately 38.5 psu in both areas) in late spring/early summer. The σ_θ seasonal signal is roughly the inverse of the temperature signal, with the densest water (σ_θ = 26-27 kg m^{-3})

appearing in winter whereas the lowest density water (24-25 kg m^{-3}) is seen in late summer/early autumn. The σ_θ data also reveal a seasonal variation in density vertical stratification over the upper 50 m characterized by nearly uniform σ_θ in winter and stronger stratification over the rest of the year. During all seasons, the top of the main pycnocline, roughly marked by the 26 σ_θ contour, appears at about 50 m depth (Fig. 2).

Seasonal θ-S diagrams (Fig. 3a-d) clearly show a yearly progression in vertical stratification in the survey region. The σ_θ range over the vertical extent of the surveys is greatest during summer, extending from roughly 23.5 kg m^{-3} at the surface to 28.45 kg m^{-3} at 200 m. During summer, the density stratification in the upper 50 m, above σ_θ = 26 kg m^{-3}, is largely due to temperature stratification. The σ_θ range observed during autumn is slightly smaller, 23.9-28.5 kg m^{-3}. The higher near-surface densities of autumn relative to summer are principally due to the higher salinities observed in autumn. At σ_θ < 26 kg m^{-3}, salinities of the autumn surveys are roughly 0.5 psu greater than those of the summer surveys. The near-surface layer of strong temperature stratification seen in the summer and autumn surveys is absent during the winter surveys. The weak vertical temperature stratification observed in winter results in weak vertical density stratification, with σ_θ varying by about 0.5 kg m^{-3} in the upper 50 m. Near-surface vertical temperature and density gradients are slightly greater during the spring surveys, signaling the formation of the seasonal thermocline. It's noteworthy that during all seasons the largest temporal variations in θ, S and σ_θ occur above the permanent pycnocline (roughly at σ_θ< 26 kg m^{-3}), with much smaller variations of these properties seen in the permanent pycnocline and below.

3.1.2 Mooring and SST data

The temperature and salinity records from the mooring (Fig. 4) show seasonal signals in close agreement with those exhibited by the cruise data. In particular, the mooring data show the order 3-month shift of the seasonal signal of salinity relative to temperature. The shift is particularly well defined by the temperature and salinity maxima, which occur, respectively, in late September 2015 and mid-December 2014. However, the shift is not as well defined by the minima of temperature and salinity. The seasonal decline in temperature occurs over the autumn and early winter and terminates in a clear minimum in mid-January 2015. By contrast, the seasonal salinity decline occurs over December 2014 - March 2015 and is not followed by a

clear salinity minimum over the ensuing four months. Nevertheless, both the salinity and temperature records show a dominant seasonal signal relative to higher frequency variations. The seasonal temperature signal extends over 6°C, roughly from 25 to 31°C, while the higher frequency variations are of magnitude 2°C or less. The seasonal salinity signal is approximately 1.1 psu in magnitude, roughly from 38.7 to 39.8 psu, upon which fluctuations of order 0.4 psu are superimposed.

The distribution of θ-S derived from the mooring data (Fig. 3f) show a seasonal progression of near-surface density related to the seasonal variation of temperature and salinity. The increase in near-surface density from its minimum in October to its maximum in January is largely the product of declining temperatures, while the subsequent decline in near-surface density over January-April is principally due to a decrease in near-surface salinity. Completing the cycle, the May-October decrease in density is primarily the result of rising near-surface temperatures.

Comparing the moored temperature record with the satellite-derived SST record from the 0.25^{o} latitude by 0.25^{o} longitude cell encompassing the mooring indicates predominately well-mixed or weakly stratified conditions above the moored CTD (Fig. 4a). Significant temperature stratification above the mooring (indicated by a difference between the SST and mooring temperature) is confined to the period of early-May through mid-August. However, the near-surface stratification is eroded on a number of occasions during this period (i.e. in mid-May, early-June, and mid-July 2015). These mixing events appear to be at least partly due to the action of the surface wind stress and they correspond to peaks in the surface wind stress record derived from the NCEP winds (Fig. 4c).

The long-term (6-year) record of SST from the cell encompassing the mooring (Fig. 5a) very clearly shows the dominance of the seasonal signal over higher frequency variations. The seasonal SST signal spans a range of roughly 6^{o}C, between minima and maxima of 25 and 31^{o}C, whereas the magnitude of the higher frequency SST variations is at most 1^{o}C.

3.2 Factors controlling the seasonal signals

The observations reviewed above clearly show that the temporal variations of temperature and salinity above the permanent pycnocline in the near-shore region off of Port Sudan are dominated by seasonal signals that differ in phase by roughly 3 months (with the seasonal

277 temperature signal leading). We now consider the extent to which these seasonal signals may be
278 due to surface mass and heat flux (local processes) and to the effect of alongshore advection. We
279 focus first on the impact of local processes on the seasonal signals.
280
281 ***3.2.1 Local processes***
282 The change in mean temperature and salinity above the main pycnocline was estimated by
283 evaluating Eq. 8 and 9 with inclusion of only the first term in the integral of each equation. The
284 depth of the layer above the main pycnocline, h, was approximated as 50 m based on the
285 contoured temperature and salinity fields derived from survey data (Fig. 2).
286 The computed temperature driven by local heat flux exhibits a seasonal signal similar to
287 observed temperature fields but with the minima and maxima occurring 1-2 months later (Figs.
288 4a and 5a). In addition the computed temperature series shows a long-term decline (of roughly
289 $0.8^{o}C\ yr^{-1}$) that is not matched by the observations (Fig. 5a). This trend in the computed
290 temperature cannot be attributed to the omission of vertical mixing, as mixing with the cooler
291 water below the main pycnocline (Fig. 2) would tend to reduce near-surface temperatures even
292 further.
293 Reflecting the dominance of evaporation over precipitation, the computed salinity series
294 driven only by surface mass flux shows a steady increase with time and no vestige of a seasonal
295 signal (Figs. 4b and 5b). Altering this trend to match the salinity observations requires both a
296 long-term delivery of lower salinity near-surface water to the region as well as a mechanism to
297 produce the observed seasonal oscillations.
298
299 ***3.2.2 The effect of alongshore advection***
300 Evaluating the impact of alongshore advection on the seasonal temperature and salinity signals
301 from Eq. 8 and 9 required estimates of $V(t)$, dS/dy, and dT/dy. In estimating the latter two
302 properties, we used SODA temperature and salinity data from 2009-2010. These data show that
303 near-surface temperatures (averaged over the upper 50 m) tend to decline going northward over
304 the central and northern Red Sea (Fig. 6a). A similar trend has been observed based on analysis
305 of SST data (Raitsos et al., 2013) and hydrographic survey measurements (Neumann and McGill,
306 1962; Maillard and Soliman, 1962; Sofianos and Johns, 2007). Also shown by the SODA data is
307 a tendency for the near-surface salinity to increase going northward over the entire Red Sea (Fig.

6b), consistent with trends observed by hydrographic survey data (Neumann and McGill, 1962; Maillard and Soliman, 1962; Sofianos and Johns, 2007). To estimate *dS/dy* and *dT/dy* in our study area, we used temperature and salinity data from SODA grid cells extending between 18 and 22.5°N and arranged in roughly the alongshore direction (Figs. 6a and b). Averages (over the upper 50 m) of near-surface temperature and salinity from these cells show alongshore gradients that do not appear to vary appreciably with season (Figs. 6c and d). Based on these averages, we assigned values to *dT/dy* and *dS/dy* of -0.2/111°C km^{-1} and 0.35/111 psu km^{-1}, respectively (i.e., 0.2°C decrease and a 0.35 psu increase over a degree of latitude).

In specifying *V(t)*, we assumed that the velocity signal impacting the seasonal temperature and salinity signals varied on a similar time scale as these signals and can be expressed as

$$V(t) = a \sin\left[\frac{2\pi t}{P} + \phi\right] + V_o \qquad (10)$$

where a is the sinusoidal flow amplitude, P is the period of 1 year, V_o is the long-term mean flow and ϕ is a phase relative to the beginning of each year. Surface geostrophic velocities determined from the SLA data tend to support this form of a seasonal velocity signal in that they show a tendency for alongshore velocity to be directed northward over winter-spring and southward over summer-autumn (Figs. 4d and 5c). To assign the required parameters in Eq. 10, we used a 6-year (2009-2014) series of alongshore (N-S) geostrophic velocity determined from SLA data in the vicinity of our study area (19-20.5°N; 37.5-38°E). Applying a nonlinear least-squares regression technique (with MATLAB function *nlinfit*) to fit Eq. 10 to this time series gave estimates of a = 0.047 m s^{-1}, V_o = 0.017 m s^{-1} and ϕ = 0.136 (zero crossings at June 23 and December 23).

Inclusion of the advection terms in Eqs. 8 and 9 has two principal effects on the computed temperature and salinity series. One is that the mean influx of warmer and less saline water from the south, carried by the steady northward flow, counteracts the long-term trend of declining temperatures and rising salinities seen in the series computed with only the local surface flux terms (Figs. 4 and 5). These trends are not apparent in the series computed with the addition of the advection term. The second effect is produced by the yearly oscillation in alongshore velocity and most profoundly affects the computed salinity signal, which acquires a seasonal variation with the inclusion of the advection term (Figs. 4b and 4d).

It is unrealistic to expect a close match between the observed and computed temperature and salinity series as our crude calculation omits many factors that may influence near-surface temperature and salinity. These include, but are not limited to, mixing of water across the main pycnocline, temporal variations in the alongshore temperature and salinity gradients, differences between the actual flows and our representation of the alongshore velocity signal and the effect of across-shore advection. Nevertheless, the seasonal signals of the temperature and salinity series computed with the inclusion of the advection terms exhibit many of the features of the observed seasonal signals. In close agreement with observed temperatures, the computed temperature series has a seasonal signal spanning a range of roughly 6^{o}C, with minima close to 26^{o}C in late-winter/early spring and maxima near 32^{o}C predominately occurring in late autumn (Figs. 4a and 5a). The seasonal signal of the computed salinity series resembles observed salinity signal in that it extends over a range of roughly 1.2 psu, with maxima winter and minima in early summer (Figs. 4b and 5b). Notably, the observed 3-month phase difference between the observed seasonal temperature and salinity series (with temperature leading) is reproduced by the computed series (Fig. 5).

However there are differences between the computed and observed seasonal temperature and salinity signals worth noting. The seasonal variation of the computed temperature series is somewhat smaller (by ~ 1^{o}C) than the range of the observed temperatures (Figs. 4a and 5a). The seasonal signal of the computed salinity series roughly matches that observed at the mooring, but does not show the abrupt decline in salinity observed in February 2015 (Fig. 4b). The long-term salinity signal determined from the SPS survey data is roughly in phase with the computed salinity signal, but varies over a much smaller range (Fig. 5b). We can offer no clear reason as to why the range of the survey-averaged salinities is smaller than the range of the salinities derived from the computations and the mooring data. One possibility is that the survey-derived salinities, which are essentially point measurements, do not capture the full range of the seasonal signal as they are aliased by salinity variations on time scales shorter than that of the seasonal signal.

4. Discussion and Conclusions

As noted in Section 3.1.1, our observation is not the first of a dominant seasonal signal in near-surface temperature records from the Red Sea, as this was previously reported by Churchill et al. (2014). The similarity of the seasonal oscillations of near-surface temperature observed in our

study with those detected further to the north and on the opposite side of the Red Sea by Churchill et al. (2014) suggests that such oscillations may be a ubiquitous over the central Red Sea. Our analysis has revealed that these oscillations cannot be solely ascribed to local surface heat exchange, as this would produce a long-term heat loss and a multiyear decline in near-surface temperature. According to the results of our simple heat-flux model, the long-term trend of heat loss through surface exchange near Port Sudan is largely balanced by the advection of warmer water from the south. In our model, this advection is the product of a long-term mean northward flow, inferred from analysis of SLA fields, and a tendency for temperatures to increase going southward from Port Sudan, as deduced from SODA data. Presently, there are no published long-term velocity records to verify the existence of a long-term mean northward flow off of Port Sudan. It is noteworthy, however, that such a flow often appears in the results of hydrodynamic models of the Red Sea, taking the form of a western boundary current flowing northward over the southern and central Red Sea (Sofianos and Johns, 2003; Yao et al., 2014b; Zhai et al., 2015). The alongshore temperature gradient inferred from the SODA data is associated with a near-surface temperature maximum in the central/southern Red Sea south of Port Sudan. As noted in a review by Morcos (1970), this feature of the Red Sea surface temperature field has been recognized since the early twentieth century. More recently, it has appeared in large-scale survey data (Maillard and Soliman, 1986; Sofianos and Johns, 2007), SST fields derived from satellite measurements (Raitsos et al., 2013) and hydrodynamic model results (Sofianos and Johns, 2003). In interpreting their model results, Sofianos and Johns (2003) ascribe the surface temperature maximum to relatively weak winds in the central Red Sea area of wind convergence.

Our observations show that near-surface salinity variations off of Port Sudan are also dominated by a seasonal signal. Because of the dominance of evaporation over precipitation in the Red Sea, the observed oscillations in near-surface salinity cannot be attributed to local mass flux at the surface, as this would produce a nearly steady increase in near-surface salinity. Our simple salt-flux model indicates that this tendency for salinity to increase due to local evaporation is largely balanced by a northward flux of less saline water from the south. The trend of increasing near-surface salinity going northward over the Red Sea is commonly seen in both observations and model results (Morcos, 1970; Clifford et al., 1997; Sofianos and Johns, 2003, 2007; Yao et al., 2014a,b). This northward salinity increase has largely been attributed to the influx of relatively low salinity water into the southern Red Sea through the Strait of Bab al-

Mandeb. It is well documented that this influx takes two forms. During summer and early autumn, low-salinity water, commonly referred to as Gulf of Aden Intermediate Water, enters the Red Sea in sub-surface (30-120 m) layer (Patzert, 1974; Murray and Johns, 1997). During the rest of the year, low salinity water, commonly referred to as Gulf of Aden Surface Water, enters the Red Sea over a surface layer of order 50 m depth (Murray and Johns, 1997; Smeed, 2004).

Our analysis indicates that the yearly oscillations in near-surface salinity off of Port Sudan may be largely due to the advection of the alongshore salinity gradient by yearly oscillations of the alongshore velocity. As noted by Sofianos and Johns (2003), seasonal variations in Red Sea flow patterns are likely as in the Red Sea 'both wind and thermohaline forcing are highly variable at the seasonal timescales'. Seasonal averages of their modeled flows in the Port Sudan area are consistent with the alongshore velocity component derived from the SLA data (Fig. 5), directed northward over winter (September-May) and southward over the summer (June-August) (Figs. 4 and 5 of Sofianos and Johns, 2003).

Prominent among the flux terms not included in our analysis are those associated with vertical mixing and across-shore advection. Although we cannot estimate vertical mixing with the data used in our study, we can assert that vertical mixing through the main pycnocline would not counteract the long-term trend of declining temperatures and rising salinity associated with local heat and mass exchange through the surface. Because cooler and more saline water is found below the pycnocline, vertical mixing through the pycnocline would tend to further reduce temperature and increase salinity in near surface waters.

Given the prevalence of basin-scale eddies within the central Red Sea (Zhan et al., 2014), it is likely that eddies may frequently cause exchange of near-shore and basin water within the central Red Sea. However, because the eddy lifespan is typically 6 weeks (Zhan et al., 2014), this exchange is likely to produce temperature and salinity changes at intervals relatively short compared with the observed seasonal signals of temperature and salinity.

Although our study has provided new insight into the character and dynamics of seasonal temperature and salinity changes in the Red Sea, it has been based on limited data from a small region and has not specifically dealt with the full suite of dynamics that may influence seasonal temperature and salinity changes. For example, it remains unclear to what extent vertical mixing may influence the observed yearly oscillations of temperature and salinity. It is uncertain to what degree our findings are applicable to other areas of the Red Sea, which may experience different

seasonal currents and conditions of heat and mass exchange than in the region near Port Sudan. Perhaps most importantly, further research is required to understand how seasonal variations in temperature and salinity may be influenced by a changing climate, and how this may in turn affect the flora and fauna of the coastal Red Sea.

Acknowledgement

The SPS surveys were funded by the Norwegian Norad's Program for Master Studies and organized by IMR–RSU in Port Sudan. We thank the captain and crew of the Sudanese Marine Security Department ships, which were used for sampling. The PSH surveys were organized and funded by IMR–RSU though the local Environmental Monitoring Program. The mooring and attached instrumentation were funded by the Michelsen Centre for Research-based Innovation in Measurements Science and Technology (MIMT) in Bergen. We are grateful to the captain and crew of the Sudanese Sea Port Corporation tugboat used for deployment. We are thankful to Prof. Abdel Gadir D. El Hag and Prof. Mohamd E.A. Hamza (former directors of IMR) for their support, and also to the IMR staff for making the data collection possible.

NCEP Reanalysis II data and NOAA High Resolution SST data were obtained from the NOAA/OAR/ESRL PSD, Boulder, Colorado, USA (http://www.esrl.noaa.gov/psd/). The work I. Skjelvan and A.M. Omar was partly supported by the Research Council of Norway through MIMT. This work is part of a PhD project at GFI–UiB funded by the Norwegian Quota program.

5. References

Berman, T., Paldor, N., Brenner, S., 2003. Annual SST cycle in the Eastern Mediterranean, Red Sea and Gulf of Elat, Geophys. Res. Lett., 30, 1261, doi:10.1029/2002GL015860, 5.

Bower, A. S., Farrar, J. T., 2015. Air–sea interaction and horizontal circulation in the Red Sea. In: Rasul, N.M.A., Stewart, I.C.F. (Eds.), The Red Sea. Springer-Verlag, Berlin, pp. 329–342.

Carton, J. A., Giese, B., 2008. A Reanalysis of Ocean Climate Using Simple Ocean Data Assimilation (SODA). Mon. Weath. Rev., 136, 2999-3017.

Churchill, J. H., Lentz, S. J., Farrar, J. T., Abualnaja, Y., 2014. Properties of Red Sea coastal currents. *Cont. Shelf Res.*, 78, 51–61, doi:10.1016/j.csr.2014.01.025

Clifford, M., Horton, C., Schmitz, J., Kantha, L. H., 1997. An oceanographic nowcast/forecast system for the Red Sea, J. Geophys. Res., 102, 25,101– 25,122.

Davis, K. A., Lentz, S. J., Pineda, J., Farrar, J. T., Starczak, V. R., Churchill, J. H., 2011. Observations of the thermal environment on Red Sea platform reefs: a heat budget analysis. Coral Reefs 30:25–36.

Farrar, J. T., Lentz, S., Churchill, J., Bouchard, P., Smith, J., Kemp, J., Lord, J., Allsup, G., Hosom, D., 2009. King Abdullah University of Science and Technology (KAUST) mooring deployment cruise and fieldwork report, technical report. Woods Hole Oceanographic Institute, Woods Hole, Mass, 88 pp.

Ferrier-Pages, C., Gattuso, J., Jaubert, J., 1999. Effect of small variations in salinity on the rates of photosynthesis and respiration of the zooxanthellate coral Stylophora pistillata. Marine EcologyProgress Series 181, 309–314.

Furby, K. A., Bouwmeester, J., Berumen, M. L., 2013. Susceptibility of central Red Sea corals during a major bleaching event. Coral Reefs 32. doi: 10.1007/s00338-012- 0998-5.

Guildline, 2002. Portasal Salinometer Datasheet, Model 8410A, Guildline Instrument limited, Ontario, Canada.

Kuanui, P., Chavanich, S., Viyakarn, V., Omori, M., Lin, C., 2015. Effects of temperature and salinity on survival rate of cultured corals and photosynthetic efficiency of zooxanthellae in coral tissues. Ocean Sci. J. 50 (2), 263–268.

Large, W. G., Pond, S., 1981. Open ocean momentum flux measurements in moderate to strong winds, *J. Phys. Oceangr.*, 11, 324–336.

Maillard, C., Soliman, G., 1986. Hydrography of the Red Sea and exchanges with the Gulf of Aden in summer. Oceanologica Acta, 9 - N°3, 249–269.

Morcos, S.A., 1970. Physical and chemical oceanography of the Red Sea, Oceanography and Marine Biology Annual Review, 8**,** 73-202.

Murray, S. P., Johns, W., 1997. Direct observations of seasonal exchange through the Bab el Mandeb Strait. Geophys. Res. Lett., *24*, 2557–2560.

Neumann, A. C., McGill, D. A., 1962., Circulation of the Red Sea in early summer, Deep Sea Res., 8, 223 – 235.

Patzert, W. C., 1974. Wind-induced reversal in Red Sea circulation, Deep Sea Res., 21, 109– 121.

Raitsos, D. E., Pradhan, Y., Brewin, R. J. W., Stenchikov, G., Hoteit, I., 2013. Remote Sensing the Phytoplankton Seasonal Succession of the Red Sea. PLoS ONE 8(6): e64909. doi:10.1371/journal.pone.0064909.

Reynolds, R. W., Smith, T. M., Liu, C., Chelton, D. B., Casey, K. S., Schlax, M. G., 2007. Daily High-Resolution-Blended Analyses for Sea Surface Temperature. J. Climate, 20, 5473-5496.

SAIV, 2006. Operating manual for SAIV CTD model 204 with sound velocity and optional sensors, SAIV Company, Bergen, Norway.

Sarmiento, J. L., Gruber, N., 2006. Ocean Biogeochemical Dynamics. Princeton University Press, Princeton, NJ, USA.

Smeed, D. A., 2004. Exchange through the Bab el Mandab, Deep Sea Res., Part I, 51, 455–474.

Sofianos, S. S., Johns, W. E., 2003. An Oceanic General Circulation Model (OGCM) investigation of the Red Sea circulation: 2. Three-dimensional circulation in the Red Sea, J. Geophys. Res., 108, NO. C3, 3066, doi:10.1029/2001JC001185.

Sofianos, S. S., Johns, W. E., 2007. Observations of the summer Red Sea circulation, J. Geophys. Res., 112, C06025, doi:10.1029/2006JC003886.

Sultan, S. A. R., Ahmad, F., 1991. Long-Term Temperature and Salinity Variations near Jeddah in Relation to Certain Meteorological Factors over the Red Sea, J. K.A.U. :Mar. Sci., 2, 19-29.

Sumner, D., Belaineh, G., 2005. Evaporation, Precipitation, and Associated Salinity Changes at a Humid, Subtropical Estuary. Estuaries 28 (6), 844–855.

Wallcraft, A. J., Kara, A. B., Hurlburt, H. E., Chassignet, E. P., Halliwell, G. H., 2008. Value of bulk heat flux parametrizations for ocean SST prediction. *J. Marine Syst.* 74, 241–258.

Yao, F. C., Hoteit, I., Pratt, L. J., Bower, A. S., Zhai, P., Kohl , A., Gopalakrishnan, G., 2014. Seasonal overturning circulation in the Red Sea: 1. Model validation and summer circulation. Journal of Geophysical Research-Oceans. 119:2238-2262.

Yao, F., Hoteit, I., Pratt, L. J., Bower, A. S., Kohl, A., Gopalakrishnan, G., Rivas, D., 2014. Seasonal overturning circulation in the Red Sea: 2. Winter circulation, J. Geophys. Res. Oceans, 119, 2263–2289, doi:10.1002/ 2013JC009331.

Zhai, P., Bower, A. S., Smethie, W. M., Pratt, L. J., 2015. Formation and spreading of Red Sea Outflow Water in the Red Sea. J. Geophys. Res. Oceans 120 (9), 6542—6563, http://dx.doi.org/ 10.1002/2015JC01075.

Zhan, P., Subramanian, A. C., Yao, F., Hoteit, I., 2014. Eddies in the Red Sea: A statistical and dynamical study, J. Geophys. Res. Oceans, 119, 3909–3925, doi:10.1002/2013JC009563.

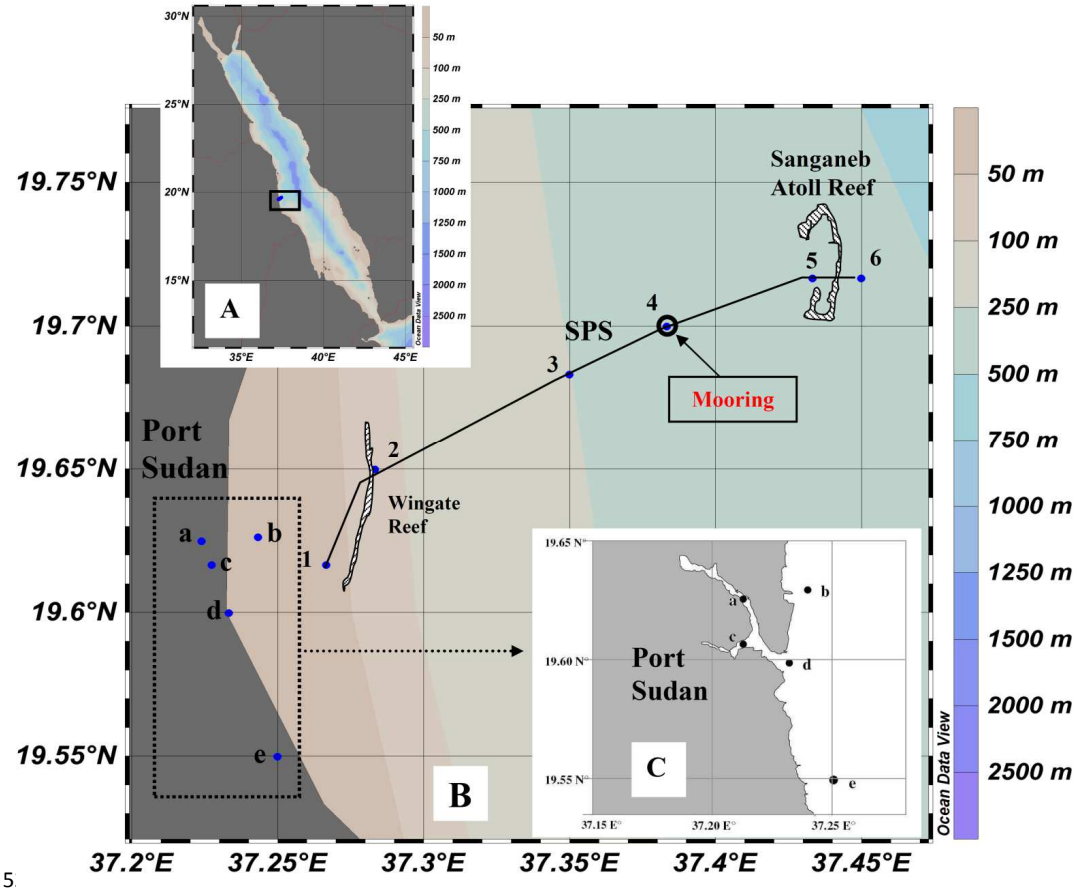

Figure 1. (A) The Red Sea with our study area enclosed in the black-bordered box. (B) Locations of our observations: the Sanganeb section (SPS; black solid line connecting six CTD stations) and Port Sudan Harbour stations (PSH; five CTD stations labelled a-e), and a CTD mooring (at the same position of station 4 in SPS). (C) PSH stations in detail: (a) IMR jetty, (b) Abu Hashish lagoon, (c) Khorkilab, (d) Harbour Inlet, and (e) Refinery stations.

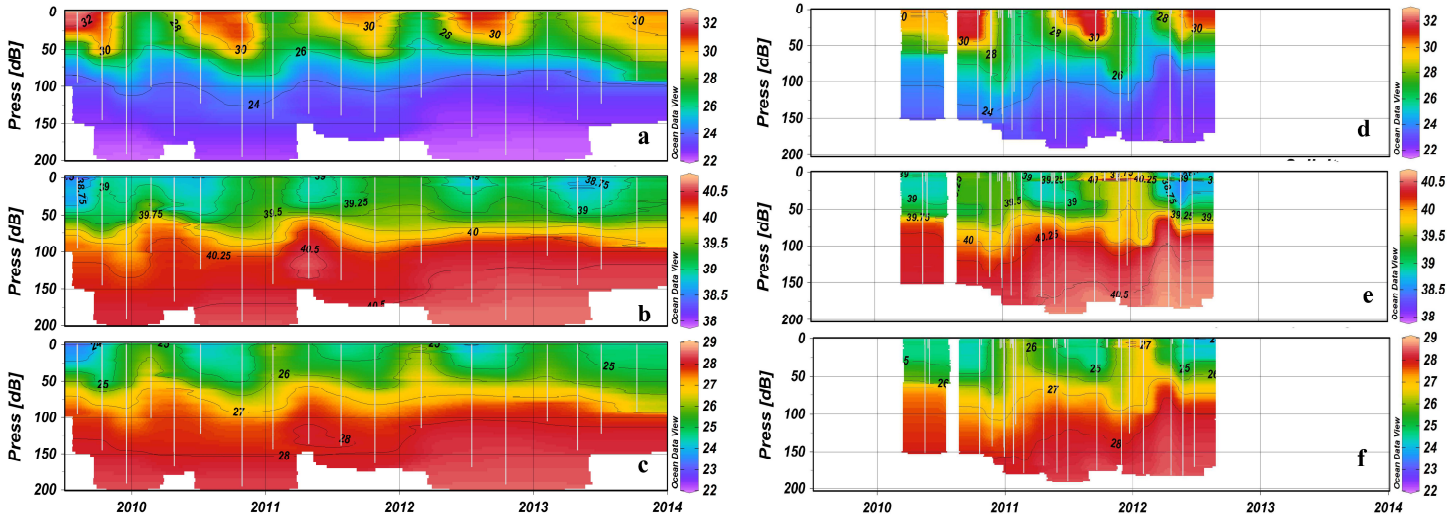

5

540 Figure 2. Depth/time contours of temperature [°C], (a) and (d), salinity [psu], (b) and (e), and potential density anomaly [σ_{θ}, kg m^{-g}],
541 (c) and (f). The left panels are averages values from the Port Sudan-Sanganeb transect (SPS; Station 1-6) and the right panels are
542 averages values from Port Sudan harbor stations (PSH; IMR jetty, Abu Hashish lagoon, Khorkilab, Harbour Inlet, and Refinery
543 stations).The vertical white lines indicate the measurements times and depth.

544

545

546

547

548

549

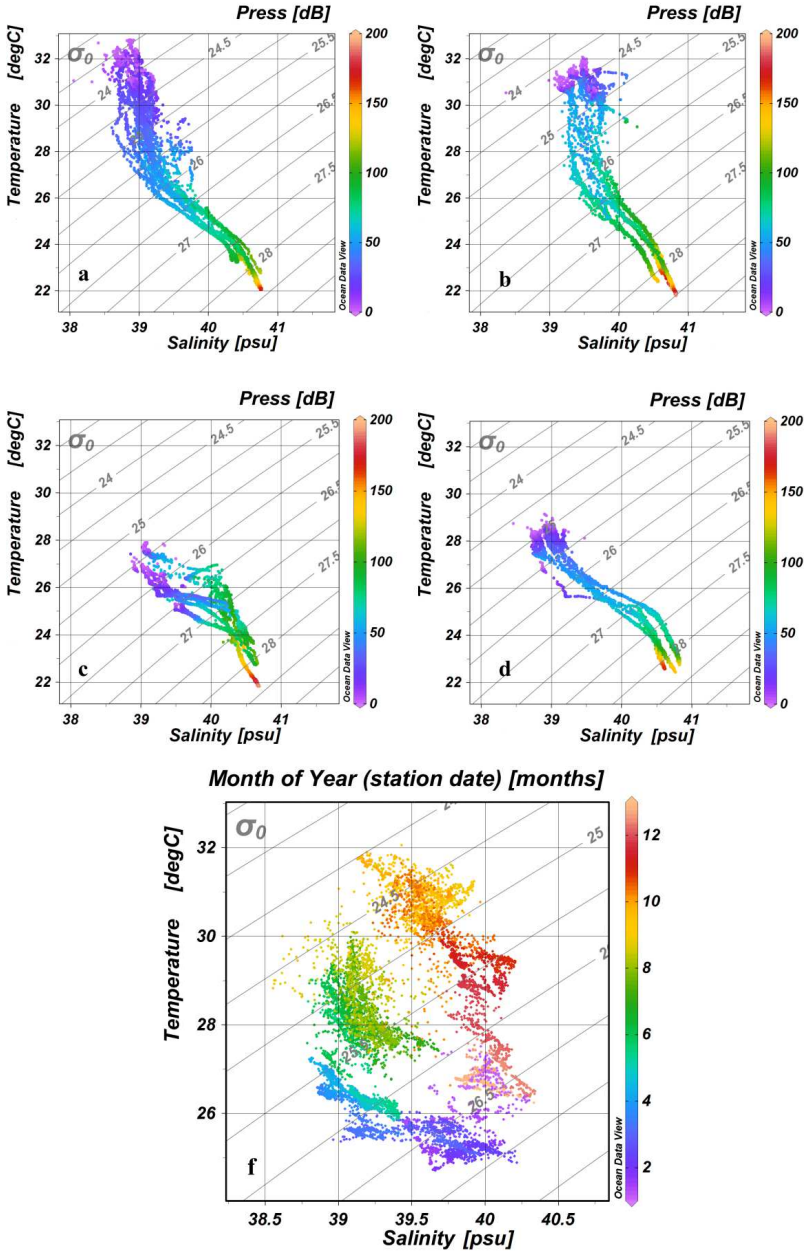

Figure 3. (a-d) T-S diagrams with seasons: (a) summer, (b) autumn, (c) winter, and (d) spring based on data from SPS. The colors indicating the depth of sampling. (f) a T-S diagram based on mooring data in which the colors indicate the month of sampling.

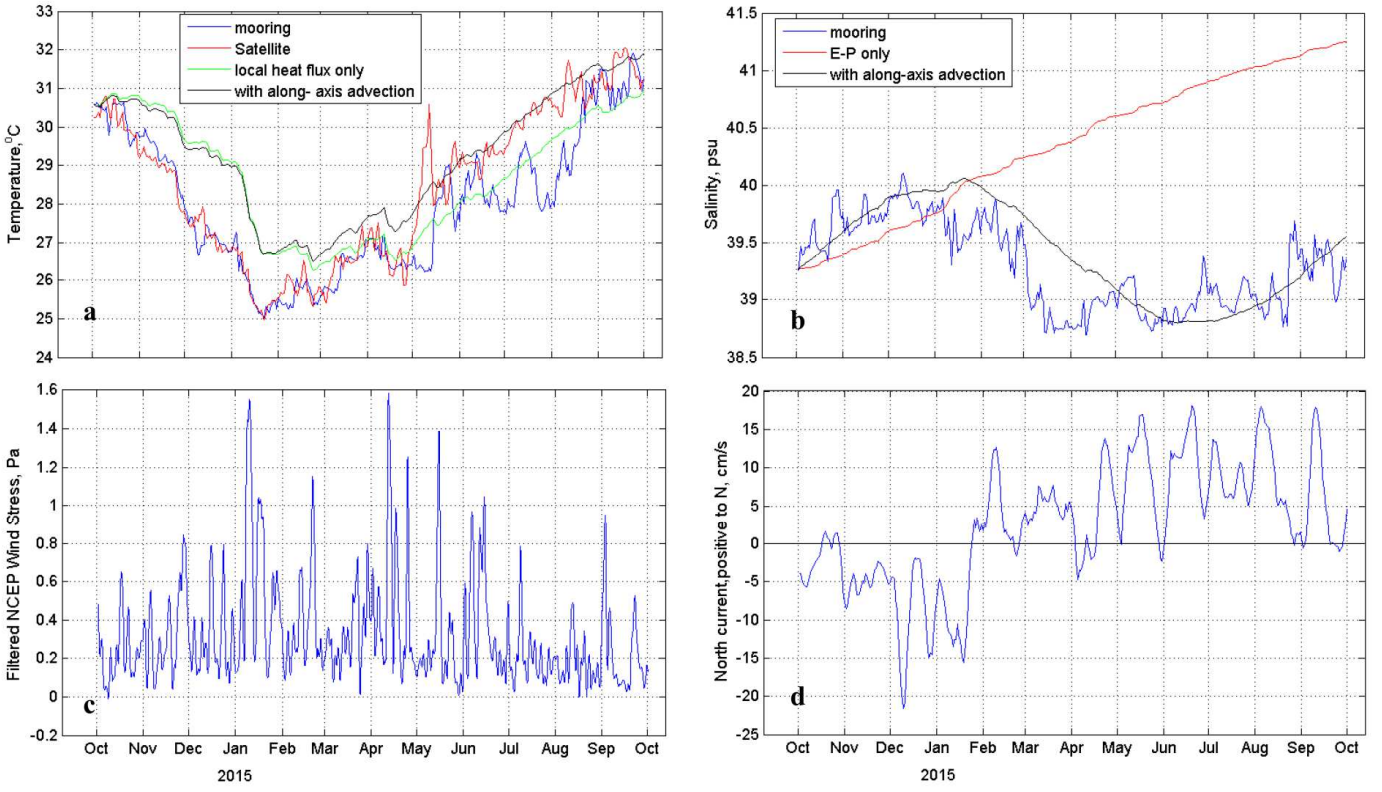

Figure 4. The seasonal variation of temperature (a), salinity (b), wind stress (c), and velocity of northward geostrophic current (d). The temperature values are from the mooring (blue line), satellite-derived (red line), computed from NCEP heat flux (green line), and computed with alongshore advection at a station close to the mooring (black line). The salinity data are from the mooring (blue line), computed based on local evaporation/precipitation (red line), and computed with alongshore advection (black line). The wind stress is calculated based on NCEP wind and filtered to 50-hour half-power period.

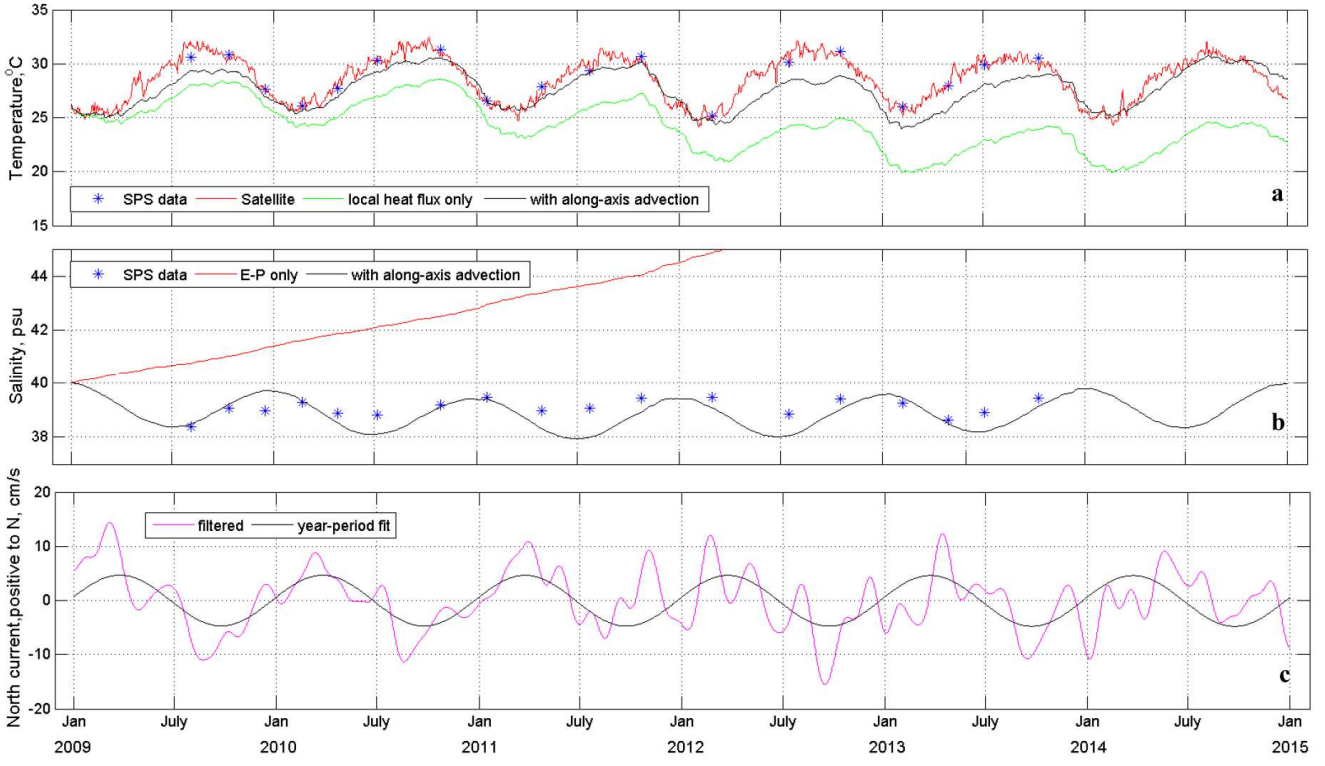

561

562 Figure 5. The seasonality of near-surface temperature (a), salinity (b), and the northward geostrophic current (c). The different temperatures
563 are; average temperature (over 50 m) from SPS data (blue stars), SST from satellite-derived data (red line), computed from NCEP heat flux
564 (green line), and calculated with alongshore advection included (black line). The different salinities are; average salinity (over 50 m) from
565 SPS transect (blue stars), calculated salinities based on local evaporation/precipitation (red line), and computed salinities with alongshore
566 advection (black line) included. Shown in (c) are the northward geostrophic current off of Port Sudan, filtered with a 50-days half-power
567 period filter (magenta line) and yearly-period velocity signal (black line).

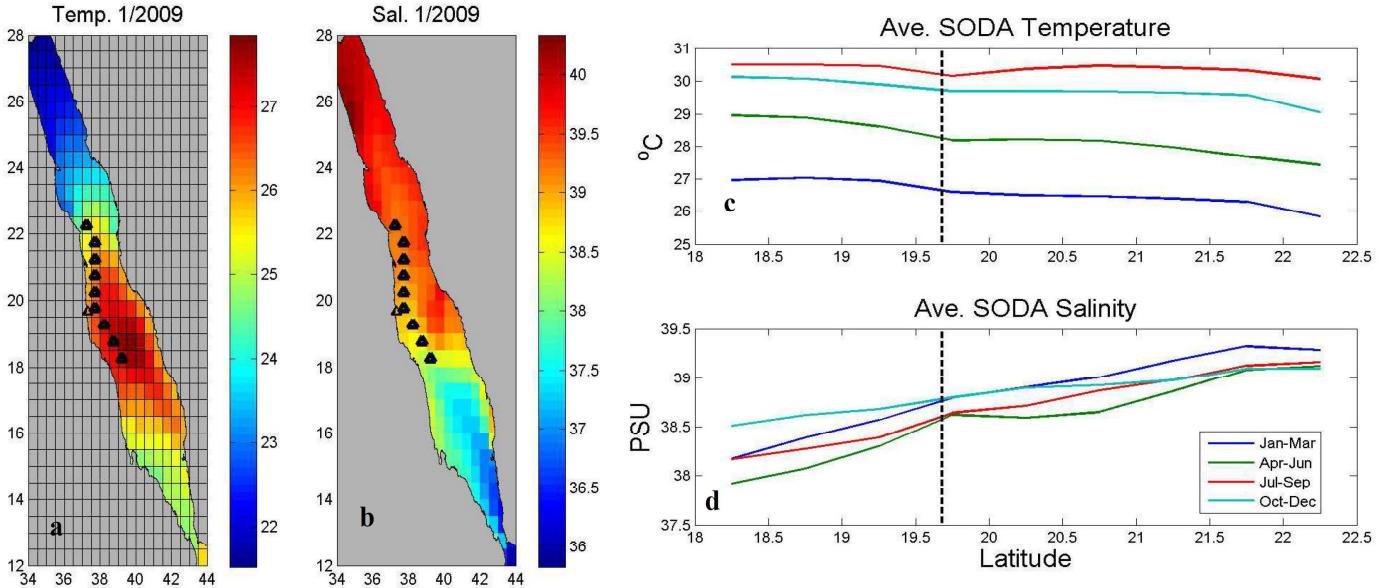

Figure 6. Properties of mean temperature and salinity, averaged over the upper 50-m, as determined from SODA data. (a) Average temperature field of Jan. 2009 with SODA grid cell indicated. (b) average salinity field of Jan 2009. The open triangle in (a) and (b) marks the location of our study's mooring. (c) and (d) Seasonally-averaged temperature and salinity (determined from 2009-2010 SODA data) at the locations shown by the closed triangles in (a) and (b).

Paper II

Dissolved inorganic carbon and total alkalinity at the Sudanese coastal Red Sea, 2009-2013

Ali, E. B., A. M. Omar, I. Skjelvan, and T. Johannessen

Submitted to Regional Studies in Marine Sciences journal

II

Dissolved inorganic carbon and total alkalinity at the Sudanese coastal Red Sea, 2009-2013

Elsheikh B. Ali[1, 2], Abdirahman M. Omar[3, 1], Ingunn Skjelvan[3, 1], and Truls Johannessen[1, 3]

[1]Geophysical Institute (GFI), University of Bergen (UiB), Bergen, Norway
[2]Institute of Marine Research (IMR), Red Sea University (RSU), Port Sudan, Sudan
[3]Uni Research Climate, Bjerknes Centre for Climate Research, Bergen, Norway

Abstract

For the first time, the seasonal variations of total alkalinity (A_T) and dissolved inorganic carbon (DIC) in the Sudanese coastal Red Sea have been studied based on a new time series collected between Port Sudan and Sanganeb reef in 2007-2013. The average surface (4 m) A_T is at its maximum during autumn/winter (2460 µmol kg^{-1}) and at minimum during spring/summer (2420 µmol kg^{-1}). The sub-surface (>10 m) A_T varies between 2452 and 2471µmol kg^{-1}, and for both surface and sub-surface, A_T correlate with salinity, which is driven by alongshore advection and local evaporation. The average DIC concentration at the surface decreases from 2080 µmol kg^{-1} during winter to 2048 µmol kg^{-1} during summer, while in the sub-surface water, the change from winter to summer is much smaller (from 2091 to 2088 µmol kg^{-1}). The DIC change is primarily driven by air-sea gas exchange caused by temperature changes, and, most likely, biological activity. The remaining change in DIC was controlled by alongshore advection and, thus, salinity variation. For surface A_T, the interannual changes were twice as much as the seasonal variations whereas for surface DIC the interannual changes were found to be less than the seasonal changes.

Keywords

Red Sea; total alkalinity; dissolved inorganic carbon; time series; seasonal variation; Sudanese coast.

1. Introduction

The ocean covers 71 % of the earth surface and thus plays a significant role in the global carbon cycle by, for instance, taking up about a quarter of the annual carbon emissions produced by the combustion of fossil fuels and production of cement (Canadell et al., 2007). The oceanic uptake of CO_2 from the atmosphere occurs primarily at high latitudes whereas in low latitude regions the ocean releases CO_2 into the atmosphere (e.g. Takahashi et al., 2009). On a regional scale, the picture is more diverse, and it is important to understand the marine carbon cycle and the processes controlling its variations, to be able to understand the diversity.

The Red Sea is located at tropical and subtropical latitudes between northeast of Africa and the Arab Peninsula. The area is not very well studied in terms of biogeochemistry and carbon cycling, and consequently not well understood. According to Souvermezoglou et al. (1989), the Gulf of Aden surface and intermediate waters are the main source of dissolved inorganic carbon (DIC), total alkalinity (A_T) and nutrients in the Red Sea. The carbon content is influenced by air-sea gas exchange, which is primarily directed from sea to air (Souvermezoglou et al., 1989; Ali, 2008) and sedimentation of calcium carbonate (Metzl et al., 1989; Souvermezoglou et al., 1989). Additionally, evaporation, primary production/remineralization of organic matter, and the formation of coral reefs are assumed to play a role in the Red Sea carbon cycle (Souvermezoglou et al., 1989), but to what extent is still poorly understood.

In the south, at 12.5°N, the Red Sea links to the Gulf of Aden and Indian Ocean through Bab Al Mandab Strait. In the north, at 28°N, the sea is divided into two branches; the Gulf of Aqaba and the Gulf of Suez, which connects the Red Sea to the Mediterranean Sea through the Suez Canal. The Red Sea is featured by high temperature, high biodiversity, and a well-developed coral reef system. Due to the high evaporation and lack of fresh water runoff, the Red Sea is considered one of the saltiest seas in the world. The salinity increases from 36.5 psu in Bab Al Mandab Strait to about 41 psu in the northern part of the sea. The average surface temperature is about 29°C and the maximum temperature zone (>30 °C) is located in the center of the Red Sea as a result of wind convergence (Sofianos and Johns, 2003).

Inorganic carbon data from the Red Sea is relatively scarce and only a few studies are focusing on carbon cycle in the open Red Sea e.g. Morcos (1970); Poisson et al. (1984); Papaud and Poisson, (1986); Metzl et al. (1989); Souvermezoglou et al. (1989); Karumgalz et al. (1990); Steiner et al. (2014); and Rushdi (2014; 2015). None of these shed lights on the temporal

variability of the carbon cycle, and studies of the carbon cycle in the western coastal regions of the Red Sea are completely lacking. In this paper, we use new time series data of hydrography and inorganic carbon collected between 2007 and 2013 in the Sudanese coastal water off of Port Sudan (Fig. 1). We first determine the seasonal changes of DIC and A_T and their relationship to hydrography followed by an estimate of the interannual changes. Then we discuss the drivers of the seasonal variability and attempt to reconstruct the complete seasonal cycles for DIC and A_T.

2. Data and Methods

2.1 Data

Two coastal datasets are used in this paper; one consists of summer data from 2007 and the other consists of seasonal data in the period between 2009 and 2013 (Table 1 and Fig.1). Both datasets were collected between Port Sudan and Sanganeb atoll reef, which is situated 30 km northeast of Port Sudan. Samples were collected at 4 m depth from 10 stations in 2007 (SPS1 section; Ali, 2008), while during 2009-2013 (SPS2 section) the samples were collected at 4 m depth from 5 stations and at 4-60 m depth from one station. Usually, the SPS2 section was sampled during October, February, April, and July. For both datasets, sampling was performed using a Hydro-Bios water sampler (2 liters) with a thermometer attached. Analyses for DIC, A_T, salinity (S), and temperature (T) were performed using standard methods (see Table 1).

2.2 Data processing

For SPS2 section, spatial variation between the surface stations has been examined with respect to temperature (SST), salinity (SSS), A_T, and DIC, and no systematic biases was found. Consequently, the average of the surface stations (4 m depth) was calculated to determine the seasonal and interannual variations.

Further, sub-surface (>10 m) data have been obtained for station 4 in SPS2 section only, and we assume that the variability measured at this station captures that of the whole section. The negligible systematic spatial variability observed in the surface as well as in sub-surface hydrographic data of SPS2 (see Ali et al., 2017) supports this assumption.

The year is divided into four seasons; summer (May to August), fall (September to November), winter (December to February), and spring (March to April). It might be argued that the summer season is too extensive; however, the fall season seasons is defined based upon when

Port Sudan receives major parts of the annual rainfall, which is in September to November (IMR, 2012).

A comparison between seasonal and interannual variations was performed by first determining the interannual changes as standard deviations (STDs), and then associate it with annual means of summer data and of winter data, separately. Then, for each season (winter and summer), we compared the STDs associated with the annual means with the average seasonal change. The interannual trend of DIC has been briefly examined for the surface and sub-surface water based on data from both SPS1 and SPS2 sections, and in this calculation the summer season was chosen due to best data coverage.

3. Results

3.1 Hydrography

The surface and sub-surface temperature and salinity measurements from station 4 in SPS2 section clearly show a seasonal signal (Fig. 2) in agreement with the more comprehensive coastal measurements thoroughly described by Ali et al. (2017). The surface temperature reaches its maxima close to 32 °C during summer and early autumn and minima of roughly 26 °C in winter. The surface salinity is lower during spring and summer (38.5 psu) compared to autumn and winter (39.0-39.5 psu), and the salinity lagged temperature with approximately 3 months. The seasonal density variation is roughly following that of salinity and is inverse of the temperature variation, with the densest water (26-27 kg m^{-3}) occurring in winter while the lowest density water (24-25 kg m^{-3}) appears in summer and autumn. During autumn and winter, the pycnocline was deeper than during summer and spring (Fig. 2c), which indicates a higher mixing during the first period.

3.2 Total alkalinity (A_T)

Surface A_T along the SPS2 section varies with the seasons as shown in Fig. 3a. However, the A_T seasonality is less clear than that observed in hydrography and there is high degree of scatter in the surface data reflecting spatial variation between the stations. Generally, the surface A_T is -at maximum during autumn and winter and at minimum during spring and summer ($\Delta A_T \approx 40$ μmol kg^{-1}), except for the years 2009 and 2010, when the maximum and minimum in A_T occurred 2-3

months earlier compared to the rest of the study period. Sub-surface A_T values vary similar to those in the surface layer (Fig. 3b), but the seasonal amplitudes decrease with depth.

Generally, the averaged surface A_T are in good agreement with those reported for the open ocean Red Sea at a similar latitude (19.5-19.9 °N) during the GEOSECS cruise in winter 1977 (2446 μmol kg^{-1}, Weiss et al., 1983) and the MEROU-I cruise in summer 1982 (2436 μmol kg^{-1}, Beauverger et al., 1984a).

The interannual variation of surface A_T (±28 μmol kg^{-1}) is greater by about two times that of the seasonal surface A_T (±15 μmol kg^{-1}), and a similar picture is seen in the sub-surface water, however, with a smaller rate between interannual and seasonal A_T variation. Furthermore, the interannual variation was larger during summer (±37 μmol kg^{-1}) than during winter (±18 μmol kg^{-1}).

A_T is a semi conservative parameter and therefore generally co-varied directly with S (Figs. 2 and 3). The correlation coefficients of the implied relationship for the area of study has been determined by linear regression between A_T and S, and the result is shown in Table 2. The regression coefficients for the surface samples are in good agreement with the results of Ali (2008) who reported a similar relationship between surface A_T and SSS (a=28.94, b=1300.2, R^2 = 0.92) based on MEROU-II data collected in October 1982 along the central axis of the Red Sea (Beauverger et al., 1984b).

3.3 Dissolved Inorganic Carbon (DIC)

Surface DIC along the SPS2 section show a clear seasonal variation, with maximum values during winter, minimum during summer, and an approximate seasonal amplitude of 32 μmol kg^{-1} (Fig. 4a). Similar to the surface A_T, also surface DIC is scattered reflecting the spatial variation between the stations. Some seasonality is also seen in the sub-surface DIC shallower than approximately 40 m, but the seasonal amplitude was lower than observed in the surface. Below 40 m, there is no clear seasonal DIC signals (Fig. 4b).

The interannual variations in the surface is stronger during summer (±6 μmol kg^{-1}) than winter, but the magnitude is much smaller than the seasonal variation (±20 μmol kg^{-1}). In sub-surface shallower than 40 m, a similar picture is seen but with a smaller rate between interannual and seasonal amplitude.

DIC is inversely correlated with SST both in surface water (R^2= 0.52), see Fig. 5, and in the sub-surface (R^2=0.6). Further, DIC also correlates with salinity, but these relationships are weaker: R^2=0.16 and 0.26 for surface and sub-surface, respectively.

The interannual trend in surface DIC based on summer values was 2.26 μmol kg^{-1} y^{-1} (R^2= 0.61), however, this result was not further explored. In sub-surface, no interannual trend was seen.

4. Discussion

In the above, we showed that the seasonal changes of DIC and A_T are taking place more or less in concert with variations in temperature and salinity. In the following, these covariations are explored in detail with the aim to gain insight into the processes that (i) are responsible for the correlations and (ii) are most influential for the seasonal variations.

4.1 DIC and A_T correlation with salinity

The significant and positive relationship between A_T and salinity (Table 2) observed both in surface and sub-surface, indicate that large part of the changes in A_T is driven by salinity variation. This finding is in agreement with the results of Millero et al., (1998) who reported that, in subtropical ocean, changes in salinity account for more than 80% of total variability in A_T. The correlation arises because A_T variability in the upper ocean is controlled mainly by processes that drives salinity changes (e.g. precipitation/evaporation) (Millero et al., 1998; Lee et al., 2006). For our data, however, salinity variation explains only about 36% of the A_T variations. This is most likely due to the fact that A_T is also impacted by calcium carbonate ($CaCO_3$) formation through pelagic and coral calcification in the Red Sea which is classified as one of the oceanic regions with the highest $CaCO_3$ production (Takahashi et al., 2014; Steiner et al., 2014).

The relationship between surface A_T and salinity in our dataset (Table 2) has a much larger positive intercept and lower slope compared to the Indian Ocean surface A_T - salinity relationship (a=68.8, b=-114) described by Millero et al. (1998). The Indian Ocean surface waters is the source water for the Red Sea, and Takahashi et al. (2014) suggests that the large intercept in the Red Sea is due to high salinity associated with $CaCO_3$ production. In addition, the change in A_T-SSS relationship can be explained partially by a loss of inorganic carbon by sedimentation in the deep water, as suggested by Metzl et al. (1989) and Souvermezoglou et al., (1989). In the deep

185 water, A_T will further decrease by remineralization of organic matter, which adds nitrate (NO_3)
186 to the water column (Elageed et al., "Oxygen and alkalinity utilization rates in the Red Sea",
187 manuscript in preparation). Furthermore, calcium carbonate precipitates may occur and reduce
188 the deep-water alkalinity even further (Ali, 2008; Rushdi, 2014; 2015). Thus, the observed
189 relationship between surface A_T and SSS is a result of mixing between fresher surface water that
190 conform to the Indian Ocean relationship in the southern Red Sea and high salinity/low A_T deep
191 water of the Red Sea (e.g. Ali, 2008; Steiner et al., 2014).

192 The correlation between DIC and salinity was positive but weaker than for A_T, which is as
193 expected due to the chemical composition of these parameters. As for A_T, mixing also influence
194 DIC but in general, biological activity and air-sea gas exchange are important contributors to the
195 variability.

196 A_T and DIC were salinity normalized (nA_T and nDIC) according to Friis et al. (2003),
197 where a constant salinity of 39 psu and an intercept of 1160 (based on data in the current study)
198 were used, see Table 2. The salinity normalization did not change the phase of the seasonal
199 variation of A_T and DIC but it slightly decreased the seasonal amplitudes of A_T and DIC. Thus,
200 even though salinity is an important factor there are also other factors contributing to the
201 variability in DIC and A_T.

202

203 **4.2 DIC correlation with SST**

204 We have found a strong anti-correlation between DIC and SST (Fig.6). A combination of
205 processes can be responsible for the observed correlation. For instance, a decrease/increase in
206 SST induces an increase/decrease in CO_2 solubility and pCO_2 difference across air-sea interface,
207 which enhances/reduces CO_2 exchange with the atmosphere. Thus, the higher the SST the lower
208 the DIC content of the ocean. The theoretical slope of this relationship can be computed for the
209 tropical ocean (see e.g. Takahashi et al., 1993) according to:

210

211 $$\frac{\partial DIC}{\partial T} = \frac{DIC_m \tau}{R} = -11 \quad (1)$$

212

213 where $\tau = \frac{\partial lnpCO2}{\partial DIC} = 0.0423$, R is the Revelle Factor (= 8 for tropical waters), and DIC_m is the
214 observed mean value (= 2060 μmol kg^{-1}). With these values, Equation (1) suggests that DIC

should decrease by 11 μmol kg^{-1} for each 1°C temperature increase. However, the observed slope in our data is only -5.23 μmol kg^{-1}, which is about half of theoretical slope, so approximately half of the change in DIC can be attributed temperature variation.

Thorough analyses of the reason why we observe only half of the expected temperature impact on DIC is beyond the data at hand. Nevertheless, one possible explanation for the discrepancy can be biological production, which is higher in the southern central Red Sea during the winter than summer due to a strong anti-cyclonic gyre centered at 19.5° N (Raitsos et al., 2013). The gyre has convergence of water at the surface and downwelling in the center. Consequently, upwelling of relatively cold sub-surface water and sinking of relatively warm surface water occur across the basin, both at coastal boundaries and away from them. This results in low productivity at the core of the gyre and higher productivity at its borders. On the contrary, low primary production during summer is caused by strong seasonal stratification (Raitsos et al., 2013). Higher primary production during winter would oppose the effect of increasing DIC expected from the decreasing temperature (see Eq. 1). During summer, primary production is low and might be surpassed by remineralization of organic matter, which increases DIC and thus opposes the decreasing DIC from increased SST. Therefore, the overall result of primary production and remineralization would be to dampen the temperature driven seasonal DIC amplitude. Therefore, we suggest that the observed DIC-SST relationship is due to air-sea gas exchange modulated by biological activity.

4.3 Influential processes for DIC and A_T seasonal variations

In the Red Sea, surface salinity, DIC, and A_T increase from south to north, while the maximum temperature zone is located and centered south of our study area (e.g. Ali, 2008). Furthermore, according to Ali et al. (2017) the geostrophic current in the coastal area off of Port Sudan directs form south to north during spring and summer bringing relatively warm and fresh water from the south, and this water is also characterized by a relatively low DIC and A_T (Ali, 2008). During autumn and winter the geostrophic current is reversed and brings waters which is colder, more saline, and richer in DIC and A_T from north. The observed seasonal changes in DIC and A_T are most likely produced by the effect of the alongshore advection superimposed on local responses to SST and SSS changes as well as biological activity.

Ali et al. (2017) examined the effect of across-shore advection on the seasonality of temperature and salinity and they found that at a seasonal time scale, the across-shore displacement signal has to be small. Based on this finding, we expect that the effect of across-shore advection on the seasonality of DIC and A_T is also small, and this is evidenced by a lack of east- or westward trends in the spatiotemporal variation between SPS1 and SPS2 stations.

4.4 Reconstruction of complete DIC and A_T cycles

Since the most influential processes for seasonal variations of DIC and A_T are identified, we attempt to reconstruct the complete seasonal patterns of DIC and A_T during the period 2009 – 2014. As a first step, DIC values ($DIC_{SST-Sat}$ in Eq. 1) was calculated by applying the DIC-SST relationship (Fig. 5) and daily satellite-derived SST data (SST_{Sat} ; NOAA High-resolution Blended Analysis of Daily SST, Version 2) extracted from 37.38° E, 19.62°N, close to the area of study. The SST_{Sat} has the same seasonal amplitude (approximately 6ºC) as the observed SST (Ali et al., 2017; their Fig. 5). The seasonality of daily $DIC_{SST-Sat}$ has the same shape as the observed DIC, higher during winter and lower during summer with a similar amplitude (~32 µmol kg^{-1}) but slightly higher values than the observed DIC, especially during summers. The daily $DIC_{SST-Sat}$ variations is about 6 µmol kg^{-1} in magnitude (Fig. 6) and these are a result of the SST variation of approximately 1ºC (Ali et al., 2017).

Next, the effect of the salinity variations on DIC was included by using a multivariate regression taking into consideration the observed surface DIC, SST, and SSS:

$$DIC_{Reg} = a\ SSS + b\ SST + c \qquad (2)$$

where the multivariate regression coefficients were: a = 6.4814, b = -4.9739, c = 1959, and R^2 = 0.54. To study the daily DIC variability we used Eq. 2, SST_{Sat} , and surface salinity (SSS_{Adv}) computed for the area in this study based on the effect of local evaporation/precipitation and alongshore advection as described in Ali et al. (2017). The resulting DIC_{Reg} has similar amplitudes as $DIC_{SST-Sat}$, which was based only on SST (Fig.6). However, when the regression was extended by salinity (as for DIC_{Reg}), the correlation coefficient (R^2=0.54) improved slightly compared to the $DIC_{SST-Sat}$ relationship (R^2= 0.52). This is partially explained by the observed phase shift between SSS and SST of approximately 3 months, which will also introduce a slight

phase shift between DIC_{Reg} and $DIC_{SST-Sat}$ (Fig.6) (Ali et al., 2017). It must be emphasized, however, that comparisons performed by Ali (2017) revealed a good correspondence between satellite-derived and measured SST whereas the computed SSS_{Adv} showed a higher degree of mismatch and varied over a much greater range than the measured SSS (Ali et al., 2017; their Fig. 5). Due to this imperfection of the SSS_{Adv}, we believe that the true potential of using Eq. 1 to estimate DIC in the study area is even greater than has been realized in Fig. 6.

The lack of a "perfect" SSS dataset also hampers the estimation of the daily variability of A_T in the study area. Nevertheless, the A_T-SSS relationship (shown in Table 2) was applied on SSS_{Adv} to estimate the complete seasonal cycle of surface A_T during the period of our survey. The computed A_T has a clear seasonal cycle resembling that observed in surface A_T (Fig. 7), high during winter and low during summer with average amplitude about 40 μmol kg^{-1}. However, as expected, there is a higher degree of mismatch compared to Fig. 6 and the computed A_T vary over a larger range. Thus, it is likely to produce an improved reconstruction of the seasonal cycle of A_T if daily SSS is used along with Equation 2.

5. Summary and Conclusion

The seasonal and interannual variations of A_T and DIC in the coastal Red Sea have been studied using a new time series collected between Port Sudan and Sanganeb reef from 2007 to 2013. Both variables show maximum values during autumn and winter, and minimum during spring and summer associated with the maxima and minima of salinity. Temperature is at maximum during summer and at minimum during winter. There are positive linear relationships between A_T and salinity and between DIC and salinity, although the latter is relatively weak, indicating that salinity is an important driver primarily for A_T variations.

The occurrence of high DIC values in winter, when primary production is normally at its highest, indicates that the consumption of DIC by primary production is less than the increase of DIC from air-sea gas exchange. The remaining changes of DIC are caused by alongshore advection during autumn and winter. The geostrophic current directs from north to south bringing relatively cold and saline water enrich with carbon to the area of study, while during spring and summer the current is reversed and transports warm and fresh water characterized with relatively low DIC from the south.

Interannual variations of A_T and DIC have been briefly examined, and for surface A_T, these changes were twice as much as the seasonal variation whereas for surface DIC, the interannual changes were found to be less than the seasonal changes.

In conclusion, seasonal DIC variations are governed by, in decreasing order, temperature driven air-sea gas exchange, biological activity, and alongshore advection. Whereas A_T variations are driven mainly by salinity, which is directly controlled by local processes such as evaporation/precipitation in addition to alongshore advection.

Acknowledgement

The SPS1 survey is the fieldwork of Ali's master thesis (2008) funded by Quota program at University of Bergen, while the SPS2 survey was funded by the Norwegian Norad's Program for Master Studies (NOMA) and organized by Institute of Marine Research (IMR) at Red Sea University (RSU) in Port Sudan. All cruises operating the SPS2 transect have been conducted on the Sudanese Marine Security Department ships. We are thankful to the former director of IMR: Prof. Abdel Gadir D. El Hag for his support and to all IMR staff for making the time series collection possible. Also, thanks to Solveig Kringstad the former senior engineer at Geophysical Institute - University of Bergen for her great efforts in analyzing the samples. NOAA High-resolution Blended Analysis of Daily SST, (Version 2) data were obtained from the NOAA/OAR/ESRL PSD, Boulder, Colorado, USA (http://www.esrl.noaa.gov/psd/). The work of A.M. Omar and I. Skjelvan has been partly supported by the Research Council of Norway through The Michelsen Centre for Industrial Measurement Science and Technology. This work is part of a PhD project at GFI–UiB funded by the Norwegian Quota program.

6. References

Ali, E. B., 2008. The inorganic carbon cycle in the Red Sea, Master's thesis, Geophysical Institute, University of Bergen, Bergen, Norway, 77 pp.

Ali, E. B., Churchill, J. H., Barthel, K., Skjelvan, I., Omar, A. M., de Lange, T. E., and Eltaib, E. B. A., 2017. Seasonal and interannual variations of hydrographic parameters in the Sudanese coast of the Red Sea, 2009-2015, submitted to Regional Studies in Marine Sciences journal.

Beauverger,C., Brunet, C. Poisson, A. 1984a. MD 33/MEROU a bord du "MARION DUFRESNE" 16 juin au 4 juillet 1982,25 septcmbre au 4 octobre 1982. Les rapports des campagnes ala mcr, publication des T.A.A.F. No. 82-04, 181 pp.

Beauverger,C. 1984b. MD 33/MEROU a bord du "MARION DUFRESNE"]6 juin au 4 juillet 1982,25 septembre au 4 octobre 1982. Les rapports des campagnes a la mer, publication des T.A.A.F. No. 82-05,163 pp.

Canadell, J. G., Le Qu´er´e, C., Raupach, M. R., Field, C. B., Buitenhuis, E. T., Ciais, P., Conway, T. J., Gillett, N. P., Houghton, R. A., and Marland, G., 2007. Contributions to accelerating atmospheric CO_2 growth from economic activity, carbon intensity, and efficiency of natural sinks, P. Natl. Acad. Sci. USA, 104, 18353– 18354.

Dickson, A. G., Sabine, C. L., Christian, J. R., 2007. Guide to best practices for ocean CO_2 measurements, p. 191. PICES Special Publication 3.

Elageed et al., 2017. Apparent oxygen and alkalinity utilization rates in the Red Sea, in prep.

Friis, K., Körtzinger, A., Wallace, D. W. R., 2003. The salinity normalization of marine inorganic carbon chemistry data, *Geophys. Res. Lett.*, 30, 1085, doi:10.1029/2002GL015898.

IMR, 2012. Environmental Baseline Study for Mersa El-Sheikh Ibrahim, conducted by Institute of Marine Research (IMR) in coloration with Faculty of Marine Sciences and Fishers (FMSF) at Red Sea University (RSU), Port Sudan, Sudan.

Johnson, K. M., Wills, K. D., Butler, D. B., Johnson, W. K., and Wong, C. S., 1993. Coulometric total carbon dioxide analysis for marine studies, Mar. Chem., 44, 167–187. 1993.

Krumgalz, B.S., Erez, J., Chen, C.T.A., 1990. Anthropogenic CO2 penetration in the northern Red Sea and in the Gulf of Elat (Aqaba), Oceanologica Acta, 13 (3), 283-290.

Lee, K., Tong, L. T., Millero, F. J., Sabine, C. L., Dickson, A. G., Goyet, C., Park, G. H., Wanninkhof, R., Feely, R. A., Key, R. M., 2006. Global relationships of total alkalinity with salinity and temperature in surface waters of the world's oceans, Geophys. Res. Lett., 33, L19605, doi:10.1029/2006GL027207.

Metzl, N., MooreIII, B., Papaud, A., Poisson, A., 1989. Transport and carbon exchange in Red Sea inverse methodology, Global Biogeochemical Cycle, Vol. 3, No. 1, pages 1-26.

Millero, F. J., Lee, K., Roche, M., 1998. Distribution of alkalinity in the surface waters of the major oceans, Mar. Chem., 60, 111 –130.

Morcos, S.A., 1970. Physical and chemical oceanography of the Red Sea, Oceanography and Marine Biology Annual Review 8 pp. 73–202.

Papaud, A., Poisson, A., 1986. Distribution of dissolved CO_2 in the Red Sea and correlation with other geochemical tracers, J. Mar. Res., 44, 385-402.

Poisson, A., Morcos, S.A., Souvermezoglou, T., Papaud, A., Lvanoff, A., 1984. Some aspects of biogeochemical cycles in the Red Sea with special reference to new observations made in summer 1982, Deep Sea Res. Part A. Oceanographic Res. Paper, Vol.31, Issue 6-8, 707-718.

370 Raitsos, D. E., Pradhan, Y., Brewin, R. J. W., Stenchikov, G., Hoteit, I., 2013. Remote Sensing
371 the Phytoplankton Seasonal Succession of the Red Sea. PLoS ONE 8(6): e64909.
372 doi:10.1371/journal.pone.0064909.
373 Rushdi, A. I., 2014. Calcium carbonate saturation levels of the Red Sea coast of Yemen and
374 biogeochemical effects of excess CO2. In: International conference on the marine
375 environment of the Red Sea, King Abdulaziz University, Jeddah, 10–13 Nov 2014 (in press).
376 Rushdi, A.I., 2015. Calcite and Aragonite Saturation States of the Red Sea and Biogeochemical
377 Impacts of Excess Carbon Dioxide, in: Rasul, N.M.A., Stewart, I. C.F. (Eds), The Red Sea
378 the Formation, Morphology, Oceanography and Environment of a Young Ocean Basin,
379 Springer Earth System Sciences, ISBN 978-3 662-45201-1(eBook), DOI 10.1007/978-3-
380 662-45201-1.
381 Sofianos, S. S., Johns, W. E., 2003. An Oceanic General Circulation Model (OGCM)
382 investigation of the Red Sea circulation: 2. Three-dimensional circulation in the Red Sea, J.
383 Geophys. Res., 108, NO. C3, 3066, doi:10.1029/2001JC001185.
384 Souvermezoglou, T., Metzel, N., Poisson, A., 1989. Red Sea budgets of salinity, nutrients and
385 carbon calculated in the Strait of Bab Al Mandab during summer and winter seasons, Journal
386 of Marine Research, 47,441-456.
387 Steiner, Z., Erez, J., Shemesh, A., Yam, R., Lazar, B., 2014. Basin-scale estimates of pelagic and
388 coral reef calcification in the Red Sea and Western Indian Ocean, PANS, Vol. 111, No. 46,
389 16303-16308.
390 Takahashi, T., Olafsson, J., Goddard, J., Chipman, D.W., Sutherland, S.C., 1993. Seasonal
391 variation of CO2 and nutrients in the high-latitude surface oceans: A comparative study.
392 Glob. Biogeochem. Cycles 7, 843–878.
393 Takahashi, T., Sutherland, S.C., Wanninkhof, R., Sweeney, C., Feely, R. A., Chipman, D.W.,
394 Hales, B., Friederich, G., Chavez, F., Sabine, C., and others. 2009. Climatological mean and
395 decadal change in surface ocean pCO2, and net sea-air CO2 flux over the global oceans. Deep
396 Sea Research Part II 56(8–10):554–577.
397 Takahashi, T., Sutherland, S. C., Chipman, D. W., Goddard, J. G., Ho, C., Newberger, T., and
398 others. 2014. Climatological distributions of pH, pCO2, total alkalinity, and $CaCO_3$
399 saturation in the global surface ocean, and temporal changes at selected locations. Mar.
400 Chem. 164:95–125.

Weiss R. F., Broecker, W. S., Craig, H. B., Spencer, D. W, 1983. Geosecs Indian Ocean Expedition, 5. Hyd. data. Nat. Sc. Fond., U.S. Government Print. Off.

Tables

Table 1: Methods of analysis

Parameters	Methods	Instrument	Accuracy
T	Temperature sensor	SAIV CTD model 204	± 0.01°C
S	Inductive cell conductivity sensor (salinity calculated from conductivity)	SAIV CTD model 204	± 0.02 mS cm^{-1}
A_T	Open potentiometric titration (Dickson et al., 2007)	Marianda VINDTA 3S	±1 µmol
DIC	Gas extraction of acidified water samples followed by coulometric titration method (Johnson et al., 1993; Dickson et al., 2007)	VINDTA 3C with UIC Coulometer (CM5012)	±0.5µmol*

* The accuracy was achieved by using certified reference material (CRM) supplied by prof. Andrew Dickson of Scripps Institution of Oceanography, USA.

Table 2: Regression ccoefficients of A_T-salinity relationship

A_T-S relationship at:	a	b	R^2
surface	32.9	1160	0.36
Sub-surface	26.4	1417	0.36

Figures

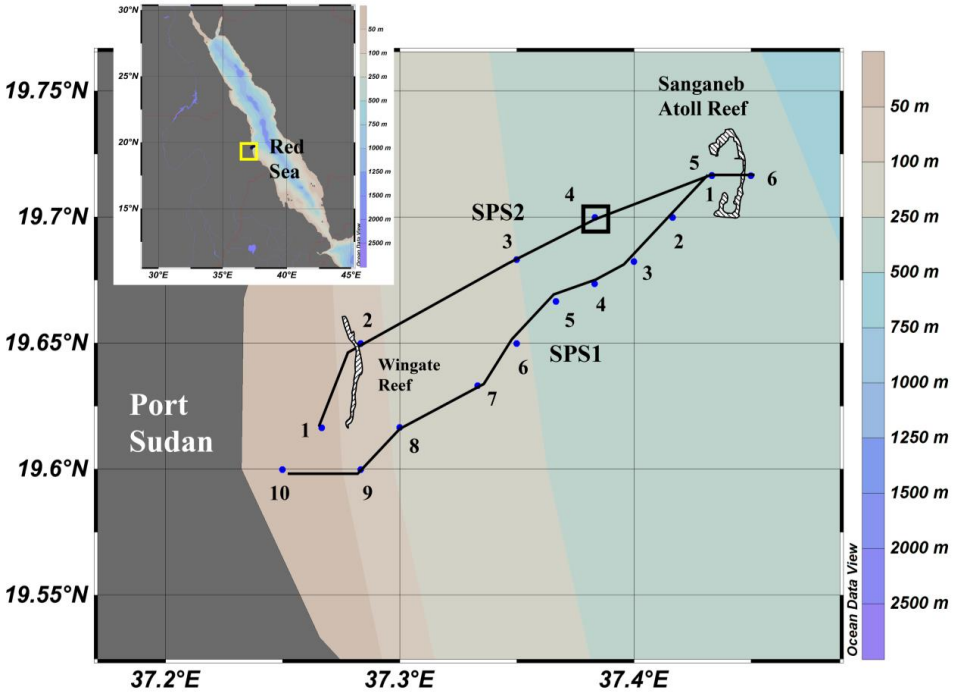

Fig. 1: The location of the coastal stations between Port Sudan and Sanganeb atoll reef. The SPS1 section is made up of ten stations (southern line) and the SPS2 section contains 6 stations (northern line). Station 1 at SPS1 section and station 5 at SPS2 section are located at the same position. Sampling depth from all stations are 4 m, except for station 4 at SPS2 section (black solid square), where data were collected from several depths between 4 and 60 m.

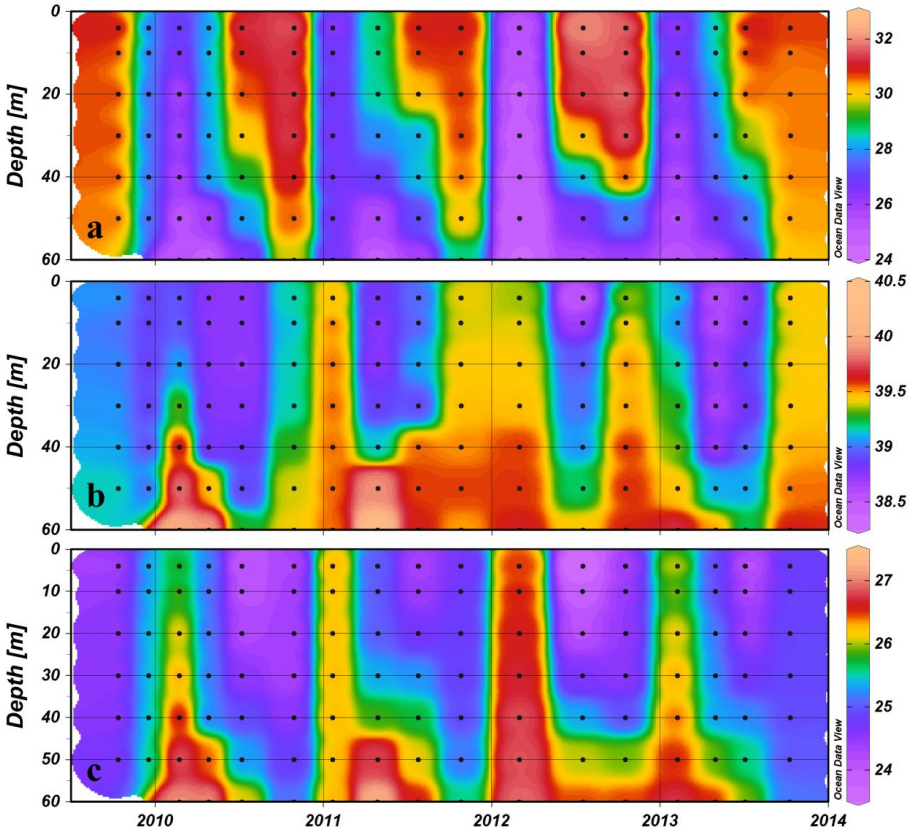

Fig. 2: Seasonal and interannual variations of water column (a) temperature [°C], (b) salinity, and (c) density [kg m^{-3}].

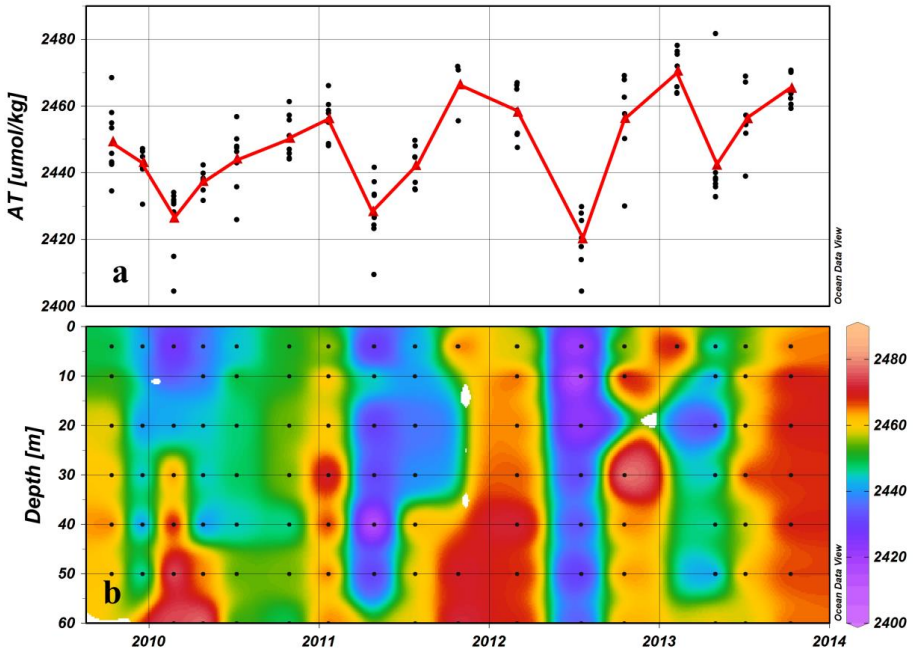

Fig. 3: Alkalinity (A_T) values [µmol kg^{-1}] (a) in the surface (station 1 to 6) and (b) in the water column (station 4). The red triangles and the line in Fig.3a indicate averaged values. All data are from the SPS2 section.

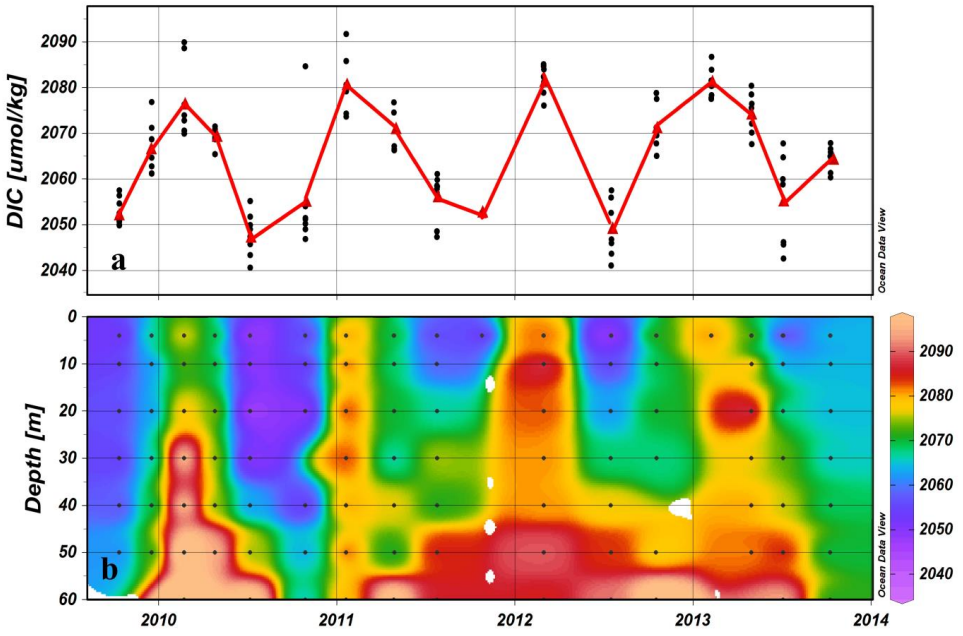

Fig. 4: DIC values [µmol kg^{-1}] (a) in the surface (station 1 to 6) and (b) in the water column (station 4). The red triangles and the line in Fig.4a indicate averaged values. All data are from the SPS2 section.

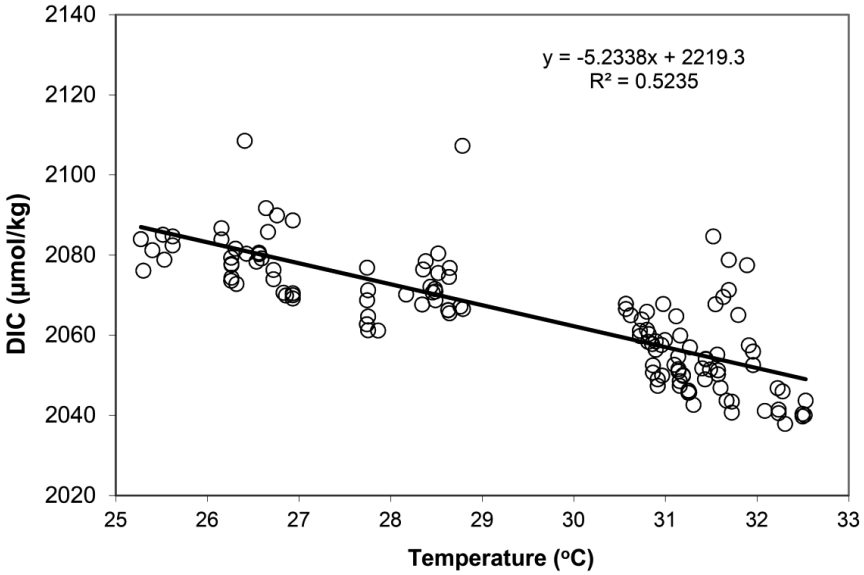

Fig. 5: Surface DIC [µmol kg^{-1}] as a function of SST [°C]. All data are from the SPS2 section.

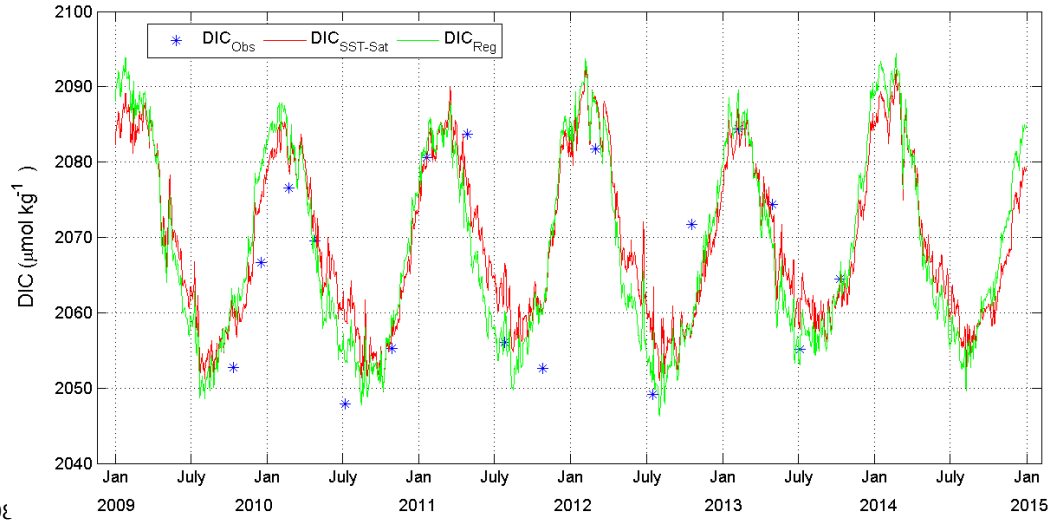

Fig. 6: The seasonal variation of computed DIC: $DIC_{SST-Sat}$ (red line) is calculated based on satellite-derived SST (SST_{Sat}) and DIC_{Reg} (green line) is calculated based on multivariate regression coefficients of the SST-SSS-DIC relationship, SST_{Sat}, and SSS_{Adv}. Blue stars indicate averaged observed surface DIC along the SPS2 section.

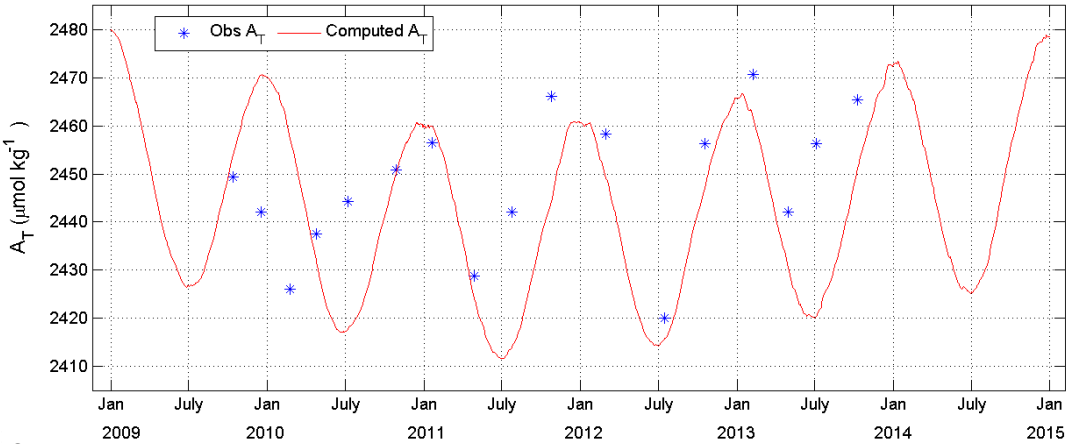

Fig. 7: The seasonal variation of the computed daily A_T (red line) based on SSS_{Adv}. Blue stars indicate averaged observed surface A_T along the SPS2 transect.

Paper III

Sea surface pCO_2 variability and air sea gas exchange in the coastal Sudanese Red Sea

Ali, E. B., I. Skjelvan, A. M. Omar, A. Olsen, T. E. de Lange, T. Johannessen, S. Elageed

Manuscript in preparation

III

Sea surface pCO2 variability and air sea gas exchange in the coastal Sudanese Red Sea

Elsheikh B. Ali[1, 2], Ingunn Skjelvan[3,1], Abdirahman M. Omar[3, 1], Are Olsen[1], Tor E. de Lange[1], Truls Johannessen[1,3], and Salma Elageed[1, 2]

[1]Geophysical Institute (GFI), University of Bergen (UiB), Bergen, Norway
[2]Institute of Marine Research (IMR), Red Sea University, Port Sudan, Sudan
[3]Uni Research Climate, Bjerknes Centre, Bergen, Norway

Abstract

Oceanic partial pressure of carbon dioxide (pCO_2^w) have been determined for the first time over a full annual cycle in the coastal Red Sea off Port Sudan. The measurements were obtained between October 2014 and October 2015 using moored autonomous sensors. pCO_2^w varies throughout the year with an amplitude of approximately 60 µatm, overlaid a high frequency signal of 10 µatm. The highest values of about 420 µatm occur during summer-autumn and the lowest values of about 360 µatm occur during winter-spring. The seasonal pCO_2^w variation is mainly incurred by temperature changes and the remaining pCO_2^w change is controlled by along-coast advection. The area is a net annual sink for CO_2 of size 24.4 mmol CO_2 m^{-2} y^{-1}. During summer and autumn, the area is a source for atmospheric CO_2, with CO_2 fluxes (F_{CO2}) of 0.1 to 2 mmol CO_2 m^{-2} day^{-1}, while during winter and spring, the area is a sink for atmospheric CO_2 of 0.02 to 5 mmol CO_2 m^{-2} day^{-1}. Based on data from the years 1977 to 2015, it is likely that during the 2000s the focus area transformed from being a net annual atmospheric source of CO_2 to a net annual sink for CO_2.

Keywords

Sea surface pCO_2; CO_2 flux; coastal Red Sea; seasonality

1. Introduction

Carbon dioxide (CO_2) is released into the atmosphere from burning of fossil fuel and land use changes. During the last decade (2006-2015) these processes have been responsible for an input to the atmosphere of 10.3 ± 0.5 Pg C y^{-1} (Le Quéré et al., 2016), of which the ocean and terrestrial biosphere have absorbed about 2.6 ± 0.5 and 3.1 ± 0.9 Pg C y^{-1}, respectively (Le Quéré et al., 2016). The global carbon budget is based on an enormous amount of data from all over the world, but there is still an ongoing effort to more precisely determine the amount of carbon exchanged between the different reservoirs.

The Red Sea is one of the under sampled areas of the world ocean. Situated between Africa and Asia, the Red Sea represents only approximately 0.12% of the world ocean surface area. It is one of the warmest and saltiest ocean areas in the world, and the biodiversity is rich, with numerous coral reefs along the coast. The area is exposed to both heavy ship traffic and climatic changes (IMR, 2012), but in spite of this, only a few studies have been conducted in the Red Sea with the carbon cycle as the main focus, and this is particularly true for the coastal areas. The GEOSECS cruise in 1977 (Weiss et al., 1983), the MEROU cruises in 1982 (Beauverger et al., 1984 a;b; Souvermezoglou et al., 1989; Metzl et al., 1989), and the MINERVE cruises in 1991, 1992, and 1999 (Metzl et al., 1995; 2008) were all conducted along the north-south central axis of the Red Sea, and all of these reported that the Red Sea was a source of CO_2 to the atmosphere. This was also confirmed by Ali (2008). The only exception to this is Metzl et al. (1995), who reported that the northern part of the Red Sea appeared to be a sink for CO_2 during summer 1991.

However, the central area of the Red Sea might not be representative for the coastal part of the sea, which is clearly seen from e.g. sea surface height anomalies which varies from coast to open ocean depending on the time of year (Yao et al., 2014), and spatiotemporal variation of primary production which is slightly higher along the coast than in the open sea (Raitsos et al., 2013). Yao et al. (2014) also reported that, for parts of the year, the coastal water was slightly fresher than in the central Red Sea.

In this study, we use new carbon and hydrography data from moored instruments deployed off the Sudanese coast of the Red Sea. The aim of the work is to determine, for the first time in this area, the air sea flux of CO_2 over a full annual cycle, and further unravel its seasonal variations and drivers.

2. Data and Methods

2.1 Data

The data used in this study are from two moored instruments deployed in October 2014 and retrieved one year later, in October 2015. The mooring site, (37.395 °E, 19.720 °N), is located 18 km north east of Port Sudan at the Sudanese coast (Fig. 1), located at the same position as one of the stations (St4) in a time series between Port Sudan and Sanganeb atoll reef presented in Ali et al. (2017a; 2017b). The moored instruments consisted of a Sea Bird MicoCat temperature (accuracy ± 0.01°C) and conductivity (accuracy ± 0.02 mS cm^{-1}) sensor (SBE 37-SM), and a SAMI-CO_2 instrument (Submersible Autonomous Moored Instrument CO_2 sensor, Sunburst Sensors, accuracy ± 3 µatm). The bottom depth at the mooring site is about 800 m, and the MicroCat and SAMI-CO_2 were parked at 37 and 34 m depth, respectively. Temperature and conductivity were determined hourly, while the partial pressure of CO_2 (pCO_2) was measured every three hours throughout the year of deployment. The pCO_2 measurements were calibrated using discrete duplicate samples of DIC (Dissolved Inorganic carbon), and A_T (Total Alkalinity) collected from 35 and 40 m depth immediately after the mooring deployment. The DIC and A_T samples were conserved using saturated $HgCl_2$ solution, kept cold and dark, and analyzed at the Geophysical Institute, University of Bergen, Norway. DIC was determined using a VINDTA 3C with UIC Coulometer (CM5012, accuracy ± 0.5 µmol kg^{-1}) based on gas extraction of acidified water samples methods followed by coulometric titration (Johnson et al., 1993; Dickson et al., 2007), while A_T was analyzed using Marianda VINDTA 3S (accuracy ± 1 µmol kg^{-1}). The accuracy was achieved by using certified reference material (CRM) supplied by prof. Andrew Dickson, Scripps Institution of Oceanography, USA. Averages of measured DIC and A_T from 35 and 40 m depth were used to calculate pCO_2 through the CO2SYS program (Pierrot et al., 2006) with the carbon system constants of Merbach et al. (1973) refitted by Dickson and Millero (1987). The computed pCO_2 were compared with the pCO_2 measurements and an adjustment of -6 µatm was applied to the observed pCO_2 data.

Atmospheric xCO_2 measurements from the nearest station (Sede Boker in Negev desert, Israel) have been downloaded from NOAA/CMDL (http://cdiac.ornl.gov/trends/co2/cmdl-flask/wis.html), and atmospheric pCO_2 values were calculated according to Körtzinger (1999).

The net air-sea CO_2 flux (F_{CO2}) was determined using the pCO_2 difference between the seawater and atmosphere:

$$F_{Co_2} = KS(pCO_2^{seawater} - pCO_2^{atmosphere}) \quad (1)$$

where K is the gas transfer velocity and S is the solubility of CO_2 in the seawater. For low wind speeds, K relationship do not have a big impact on the calculated fluxes (e.g. Sweeney et al., 2007), but at wind speeds above approximately 5 m s^{-1}, the deviation between K's becomes notable. Here, K from Nightingale et al. (2000) was used, which is relatively similar to that from Sweeney et al. (2007) for wind speeds below 10 m s^{-1}. The wind at 10 m height above sea surface, U_{10}, was calculated from daily averaged 6-hourly u- and v-wind velocity components extracted from NCEP/NCAR reanalysis 2 data at the position 20.00 °N and 37.50 °E. S from Weiss (1974) was used.

2.2 Data processing

Ali et al. (2017a) examined in detail the seasonality of the water masses with respect to temperature and salinity along their sections SPS1 and SPS2 between Port Sudan and Sanganeb atoll reef. They found that the mixed layer depth (MLD) in the area of study was approximately 40 m deep during most of the year and deeper during winter mixing. The water shallower than 40 m is part of a homogeneous surface layer, and thus, the mooring data from 37 m depth in the current study are defined as surface data.

At a few occasions, the moored instruments were dragged down to larger depths than 37 m, apparent from the Sea Bird MicroCat pressure values. This happened e.g. in the end of July and end of September 2015, however, no noticeable change was observed in pCO_2 during these times, and consequently, these data were included in the analyses.

The summer season is defined as the months May – August while the winter are the months December – February as in Ali et al. (2017b). The transitions from winter to summer and from summer to winter are referred to as spring and fall, respectively, and the fall season is when Port Sudan receive the major parts of the annual rainfall.

3. Results

The temperature and salinity data for the period between October 2014 and October 2015 is shown in Fig. 2a and 2b and have also been described in detail by Ali et al. (2017a). The seasonal temperature change was about 6°C while that of salinity was approximately 1.1 psu. The highest temperatures occurred during autumn and the lowest at the end of January, while the summer was a transition period with relatively large variations over short time. In mid-May, the temperature abruptly increased to its average summer value of 28.5°C. The salinity (Fig. 2b) was highest (around 39.7 psu) during autumn and winter and lowest (around 39.0 psu) during spring and summer. Several abrupt and large changes in salinity occurred, e.g. in early March and in late August (Fig. 2b). The seasonal peaks and lows for the salinity lagged those for temperature by about 3 months, which, according to Ali et al. (2017a) most likely is caused by temperature variation being governed by air-sea heat exchange in addition to horizontal fluxes associated with advection of water along the coast. This process partly explain the salinity variation, but in addition, the salinity is controlled by evaporation/precipitation. However, the fresh water runoff into the Red Sea is limited and the evaporation dominates over precipitation

The oceanic pCO$_2$ (pCO_2^w) showed similar seasonal pattern as the temperature (Fig. 2c), with a seasonal amplitude of approximately 60 µatm, and an induced higher frequency signal of about 10 µatm. The highest pCO_2^w occurred during autumn (400-420 µatm) when the water was warmest and saltiest, while the lowest pCO_2^w was observed in January (ca. 350 µatm) when the water was coldest. During spring, the pCO2w value was relatively stable as for temperature and to some degree also salinity. Abrupt pCO_2^w changes occurred during mid-May and early of January, where the latter had character of being an extreme event, possibly connected to both temperature and wind speed.

The atmospheric pCO$_2$ (pCO_2^{air}) (Fig. 2c) was highest during winter and spring and lowest during summer. The seasonal atmospheric amplitude was about 15 µatm, i.e. 25% of that of pCO_2^w of 60 µatm. pCO_2^{air} was lower than pCO_2^w during summer and autumn and higher than pCO_2^w during winter and spring. The seasonal cycle of ΔpCO_2 (Fig. 2d) resembled that of pCO_2^w and positive ΔpCO_2 ($pCO_2^w > pCO_2^{air}$) indicates that CO$_2$ was directed from sea to air while negative values indicates that $pCO_2^w < pCO_2^{air}$.

The daily CO_2 fluxes (F_{CO2}) are shown in Fig. 2f, and in general, the F_{CO2} values were relatively low, which was a result of low wind speeds during parts of the year in addition to periods of nearly CO_2 equilibrium between ocean and atmosphere. For the period between October and November 2014, the ocean was supersaturated with CO_2 (ΔpCO_2 positive) and an amount of up to 1.8 mmol CO_2 m^{-2} day^{-1} was degassed to the atmosphere. During winter 2015, a significant CO_2 undersaturation (ΔpCO_2 of -20 to -47 µatm) developed and the area was characterized as a sink for atmospheric CO_2 with fluxes of up to -5 mmol CO_2 m^{-2} day^{-1} during mid-January. The strongest ingassing occurred during events of high wind speeds (Fig. 2e). From February to April 2015, the surface water was slightly undersaturated with CO_2 (ΔpCO_2 varied between zero and -20 µatm) and the F_{CO2} ranged between -0.02 and -1.2 mmol CO_2 m^{-2} day^{-1}. From mid-May until October 2015, the sea surface again became a source for CO_2, of size 0.13 to 1.8 mmol CO_2 m^{-2} day^{-1}, with peaks related to peaks in the wind speed.

4. Discussion

The main hydrographic and biogeochemical drivers influencing the annual cycle of pCO_2 are discussed in Section 4.1, while Section 4.2 focuses on the long-term trend in air-sea CO_2 exchange in the Red Sea over a period of nearly four decades from 1977 to 2015.

4.1 Factors controlling pCO_2^w

pCO_2^w is affected by changes in temperature, dissolved inorganic carbon (DIC), alkalinity (A_T), and to a minor degree salinity, whereas biological production affects pCO_2^w through changes in DIC. The seasonal variability of DIC and A_T is thoroughly described in Ali et al. (2017b) where they used a new coastal time series off Port Sudan to unravel the carbonate system in this area. They found that DIC variations were mainly governed by temperature driven air-sea gas exchange modulated by biological activity, while A_T was controlled primarily by evaporation/precipitation driven salinity changes. Most of the remainder of the DIC and A_T variations are a result of advection of water masses along the coast (Ali et al., 2017b).

4.1.1 pCO_2 versus temperature

Within the range of the observed seasonal temperature change (ca. 6°C), the relationship between pCO_2^w and temperature is nearly linear. However, a more general exponential expression is used similar to the thermodynamic relationship of Takahashi et al. (1993). From mooring observations, daily pCO_2^w versus daily SST gives the relationship

$$ln\, pCO_2^w = ln\ (233) + 0.018 * SST, (R^2 = 0.60) \quad (2)$$

The proposed relationship accounts for 60% of the variability between pCO_2 and SST, and the relationship also indicate that pCO_2^w changes by 1.8% per °C. The weekly pCO_2^w versus weekly SST was also analyzed (not shown) to check if the high frequency pCO_2^w variations overlaid the pCO_2^w signal did affect the correlation between pCO_2^w and SST. This exercise gave a similar relationship as in Eq. 2 but with better correlation coefficient (R^2= 0.67) most likely due to smoothening. A theoretical value of the pCO_2^w versus temperature change was also calculated from typical coastal Red Sea data (SST = 28°C, SSS = 39 psu, DIC = 2065 µmol kg^{-1}, A_T = 2440 µmol kg^{-1}), the software CO2SYS (Pierrot et al., 2006), and constants from Mehrbach et al. (1973) refitted by Dickson and Millero (1987). From this, an isochemical change of 3.9% in pCO_2^w per °C was estimated. This is more than twice the percentage change based on observed data but, on the other hand, slightly less than that of Takahashi et al. (1993), who, based on North Atlantic data, estimated a change in pCO_2 of 4.23% per °C at constant DIC, A_T, and salinity condition. The above calculation demonstrates that there are also other processes than temperature, which are influencing the pCO_2^w in such a way that the pCO_2^w decreases while T increases.

The seasonal change of pCO_2^w versus SST seems to have an elliptical shape, where pCO_2 during the months September towards January are below the regression line, while pCO_2 during the months February towards August are, with a few exceptions, above the regression line. The lowest pCO_2^w and SST is observed in January and highest pCO_2^w in July-August (Fig. 3). pCO_2^w during early April (380-390 µatm), is about 25 µatm higher than the late December value (ca. 360 µatm) for the same temperature (approximately 27°C). Salinity varies from approximately 39.8 psu during the first period to 38.8 psu during the last. We propose that the elliptical shape is a result of super saturation of surface water CO_2 during early summer and autumn, and CO_2 is degassed from the sea into the atmosphere. This leads to decreasing pCO_2 during late autumn and early winter,

although the temperature is still higher. During early April and late December, the averaged wind values are about the same, and consequently, F_{CO2}, which is directed from atmosphere to sea at both occasions, is controlled by ΔpCO_2. In late December, the calculated CO_2 flux into the sea is approximately -1 mmol CO_2 m^{-2} day^{-1}, while in early April this amounts to -0.3 mmol CO_2 m^{-2} day^{-1}. The most likely processes being responsible for this change in pCO_2 are (i) the CO_2 uptake by surface sea occurring during December –April (ii) and along-coast advection. Metzl et al. (1995) and Ali (2008) used MINERVE data collected in 1991, 1992, and 1999 and found that the highest surface pCO_2^w values were located in the south central Red Sea similar to the maximum SST (south of our study area). Ali et al. (2017b) observed that during early February 2015 (their Fig. 4d) the geostrophic current in the area of study was reversed from southwards along-coast to northwards, which introduced water with higher pCO_2, lower salinity, and relatively higher temperature into the coastal area.

Similar elliptical shapes of pCO_2^w versus SST were also observed in the North Atlantic subtropical gyre by Lefèvre and Taylor (2002) and in the Caribbean Sea by Wanninkhof et al. (2007). According to Lefèvre and Tylor (2002), the explanation for the shape is that during summertime, the sea surface is super saturated with respect to CO_2 and will emit CO_2 to the atmosphere, lowering the pCO_2 of the water. Thus, during fall and winter, when the water cools, the pCO_2 would decrease towards even lower values than during summer. For the Caribbean Sea, Wanninkhof et al. (2007) showed that also other processes, like biological production and fresh water addition, played a role making the ellipsoid form of the pCO_2-SST relationship.

4.1.2 pCO_2 versus DIC

There are no concurrent DIC measurements to the mooring pCO_2 data, and to examine the relationship between pCO_2^w and DIC we use a regression relationship developed in Ali et al. (2017b) based on discrete surface DIC, SST, and SSS from the coastal section SPS2 (see Fig. 1); $DIC_{Reg} = aSSS + bSST + c$ ($a = 6.4814$, $b = -4.9739$, $c = 1959$, $R^2 = 0.54$). In the current work, DIC_{Reg} is determined by evaluating the above equation using the daily temperature and salinity from the mooring. Fig. 4 shows the seasonal cycle of the computed DIC_{Reg}. There is a relative strong negative correlation (R^2=0.67) between pCO_2^w and DIC_{Reg} (Fig. 5), and this is a signature

of CO_2 source areas. In such areas, higher pCO_2 induce higher efflux of CO_2 from sea to air, and thus the surface water DIC is reduced. On the contrary, the pCO_2^w-*DIC* correlation in sink areas is positive i.e. pCO_2 increases with increasing DIC (Takahashi et al., 1993). According to Ali et al. (2017b), there is a negative correlation between DIC and temperature at the Sudanese coast, and this is in line with the observed positive pCO_2-SST correlation and estimated negative pCO_2-DIC correlation from the current work. No correlation was found between temperature normalized pCO_2^w and DIC.

4.2 Air-sea gas exchange over years

The Red Sea is located in the sub-tropical area, which is characterized globally as a net annual source area of CO_2 (Takahashi et al., 2002). The monthly average of pCO_2^{air} and pCO_2^w for the period 1977 - 2015 within the area 19 - 20°N, 37 - 39°E is shown in Fig. 6. The figure combines datasets collected in the open sea (GEOSECS 1977, Weiss et al., 1983; MEROU I&II 1982, Beauverger et al., 1984a; b; MINERVE 1991; 1992; 1999, Metzl et al. 1995; 2008) with datasets from the Sudanese coast (time series from 2007 and 2009-2013, Ali et al., 2017b; mooring data in the current study). DIC values of GEOSECS was extracted from GLODAPv2 database and the data were adjusted according to the advices on the GLODAPv2 web page (Olsen et al., 2016; Key et al., 2015). The atmospheric measurements from Sede Boker station in the Negev desert started in 1995, and to estimate an atmospheric value for 1977, we first compared atmospheric xCO_2^{air} values from Mauna Loa with the atmospheric data from the Sede Boker station. The amplitude was slightly larger at the latter station, but in spite of this, the interannual trend was similar at the two stations. Thus, it is reasonable to assume that the change in xCO_2 between 1977 and 1995 at the Israeli station was similar to the change in xCO_2 observed at Mauna Loa during the same period, i.e. 27 ppm. From this, we can estimate the atmospheric xCO_2 value at Sede Boker to be 338 ppm in 1977, which corresponded to a pCO_2^{air} value of approximately 323 µatm (Fig. 6). Then, we could, with confidence, draw a line representing the Red Sea pCO_2^{air} over the years 1977 - 2015 (Fig. 6). Over these nearly four decades, the atmospheric CO_2 content increased by 66 µatm, from 323 µatm in winter 1977 to 389 µatm in winter 2015, which is equivalent to an annual increase of 1.74 µatm y^{-1}.

The open ocean data were collected during summer and autumn except GEOSECS 1977, which was collected in December 1977, while the coastal datasets cover the whole year. Fig. 6 shows that, at least since 2009, the Red Sea switches over the year between being a sink and a source of atmospheric CO_2. During summer and autumn, pCO_2^w (open dots) are higher than pCO_2^{air} (gray dots), which indicates degassing of CO_2 during these seasons. During winter and spring, although we have few data, the pCO_2^w (black dots) are in general less than the pCO_2^{air} values, which indicate uptake of atmospheric CO_2 during these seasons. Exception to this is in December 2009 and February 2010 (SPS2 data, current study). Over the year of 2014 to 2015, the area was a net sink for atmospheric CO_2 of size 24.4 mmol CO_2 m^{-2} y^{-1}.

The sub-tropics are considered net annual source areas for atmospheric CO_2, (Takahashi et al., 2002), and at the entrance of the Red Sea CO_2 is emitted to the atmosphere during both winter and summer (Souvermezoglou et al., 1989). Thus, it is reasonable to assume that the Red Sea also should be considered a net annual source area for atmospheric CO_2. The only data that could prove such an assumption is the GEOSECS data from winter 1977 (Weiss et al., 1983). We are aware that the quality of these data is subject for discussion since a relatively large data correction had to be performed (Olsen et al., 2016; Key et al., 2015). However, if we assume that the GEOSECS data are acceptable, we can include the winter value of the one central Red Sea station from 1977 in Fig. 6, and further interpolate between all winter and spring pCO_2 data available. Based on this, we speculate that the central Red Sea has been transformed from being a source area for atmospheric CO_2 all year around to becoming an area, which is in CO_2 equilibrium with the atmosphere during parts of the year, and even, at occasions, becomes a sink for atmospheric CO_2.

So, when could such a transformation have occurred? To answer this question, we compared the interannual pCO_2^w trend lines based on summer-autumn and winter-spring data with that for the interannual pCO_2^{air} trend in Fig. 6. It appeared that the line for the pCO_2^w winter-spring trend crossed the pCO_2^{air} trend line around the year 2002, which is referred to as the time of CO_2 equilibrium between atmosphere and ocean. During summer and autumn, the pCO_2^{air} is increasing with 1.95 µatm y^{-1} (not shown), which is larger than the annual change of pCO_2^w of 1.19 µatm y^{-1}. This indicates that during summer-autumn, the area emits a decreasing amount of CO_2 to the atmosphere from one year to the next. Thus, it is reasonable to assume that in the future, equilibrium is reached between atmosphere and sea surface also during summer-autumn. The coastal Red Sea might then be converted to a sink area for CO_2 throughout the year.

As mention, the amount of winter-spring data is low, and the conclusion of the Red Sea being a CO_2 source prior to 2002 must be drawn with care. The historical winter data is from the open ocean while the coastal data is not present until 2007. Therefore, it might be that the negative CO_2 fluxes are only real in the coastal area and not in the open ocean. However, the main finding from the coastal data is still valid; that the coastal Red Sea absorbs CO_2 during the winter of the last years.

This finding is compatible with the Mediterranean Sea, which was classified as a source of CO_2 during 1980s, while in the 2000s equilibria between pCO_2^w and pCO_2^{air} was reached, and at present the ocean is considered a minor sink of CO_2 (Taillandier et al., 2012). The Red Sea is similar to the Mediterranean Sea in terms of being a semi-closed sea with relatively high temperature and salinity, and, apparently, following the same transformation from being a source area for CO_2 to becoming sink area. As both seas are being influenced by the same monsoon system especially during summer, it is reasonable to assume that the same factors driving the transformation in the Mediterranean Sea are also responsible for the source to sink transformation in the Red Sea. A similar transformation is seen in the Baltic Sea, which also was characterized as a source area for CO_2 before the industrial revolution, while during the industrialization period, the Baltic Sea appears to be both a source and a sink area for atmospheric CO_2 (Omstedt et al., 2009).

Air-sea CO_2 exchange is also influenced by increasing SST as a result of global warming. Raitsos et al. (2011a) found that the annual mean SST in the Red Sea has increased by about 0.032 °C y^{-1} for the period between 1985 and 2007. An increasing SST leads to an increase in air-sea CO_2 efflux through the changes in CO_2 solubility (Yilmaz, 2008). Over time, this will create a loss of DIC in the Red Sea. The only source for DIC to the Red Sea is from the Gulf of Aden water, and according to Souvermezoglou et al. (1989), about 21% of the DIC budget that enters into the Red Sea from the Gulf of Aden is lost by air-sea gas exchange. Thus, an increase of the CO_2 flux to the atmosphere due to warming will increase the percentage of loss by air-sea gas exchange on the total DIC budget. If the supplied CO_2 is not balanced with the consumption, this process will lead to a larger loss by air-sea gas exchange on the total DIC budget. Quantification of this has not been further elaborated.

For simplicity, the increasing atmospheric CO_2 content from burning of fossil fuel and land use changes have been neglected in the above assumption. When the increase in atmospheric CO_2 content (approximately 1.8 μatm y^{-1}) is taken into account, the picture changes slightly. During

wintertime, when the Sudanese part of the Red Sea is a sink for atmospheric CO_2, the size of the sink is assumed to increase even more with increasing SST, while during summers, when the sea is a source for atmospheric CO_2, the size of the source will be less than without warming.

Increasing SST will also induce more stratification in the upper ocean, which leads to less available nutrients and reduced primary production (Behrenfeld et al., 2006; Raitsos et al., 2011b; Taillandier et al., 2012). Low vertical mixing in CO_2 source areas like the Red Sea means less CO_2 exported from the deep layer into the surface, and consequently decreasing CO_2 levels in the surface layer. This, in turn, results in CO_2 equilibrium with the atmosphere and transformation into a sink area for atmospheric CO_2.

5. Summary and conclusion

Using a SAMI-CO_2 sensor moored at about 37 m depth in the coastal Red Sea off Port Sudan, the annual cycle of oceanic pCO_2 (pCO_2^w) was studied in the period October 2014 - October 2015. During summer-autumn, the pCO_2^w values were highest, while winter-spring was the period with lowest pCO_2^w values, and the annual amplitude of approximately 60 µatm was overlaid a high frequency fluctuation of about10 µatm. The area of study acted as a source for CO_2 during summer and autumn and a sink for CO_2 during winter and spring.

pCO_2^w is relatively strongly correlated with SST (R^2 = 0.6), which indicate that the temperature is the main driver for the changes in pCO_2^w. In addition to temperature, along-coast advection, described in details in Ali et al. (2017a; b), also contribute to the observed variability in pCO_2^w.

The area is a net annual sink for atmospheric CO_2 of size 24.4 mmol CO_2 m^{-2} y^{-1}, acting as a source during summer to fall and a sink during winter to spring. When taking into consideration data from the period 1977 to 2015, it is likely that the area transformed from being a net annual source for CO_2 to becoming a net annual sink sometimes during the 2000s, when a similar transformation was seen in the Mediterranean Sea.

In the current study, pCO_2 and air-sea gas exchange have been studied in coastal Red Sea. However, it is beyond doubt that additional coastal and open ocean data would have contributed to further unravelling of the carbon cycle in this part of the sub-tropical seas.

Acknowledgement

The mooring and attached instrumentation were funded by the Michelsen Centre for Research-based Innovation in Measurements Science and Technology (MIMT) in Bergen. We are grateful to the captain and crew of the Sudanese Sea Port Corporation tugboat used for deployment. We are thankful to Prof. Abdel Gadir D. El Hag and Prof. Mohamd E.A. Hamza (former directors of IMR) for their support, and also to the IMR staff for making this deployment possible. The work of I. Skjelvan and A.M. Omar was partly supported by the Research Council of Norway through MIMT. This work is part of a PhD project at GFI–UiB funded by the Norwegian Quota program.

6. References

Ali, E. B., 2008. The inorganic carbon cycle in the Red Sea, Master's thesis, Geophysical Institute, University of Bergen, Bergen, Norway, 77 pp.

Ali, E. B., Churchill, J. H., Barthel, K., Skjelvan, I., Omar, A. M., de Lange, T. E., and Eltaib, E. B. A., 2017a. Seasonal and interannual variations of hydrographic parameters in the Sudanese coast of the Red Sea, 2009-2015, submitted to Regional Studies in Marine Sciences journal.

Ali, E.B., Omar, A.M., Skjelvan, I., Johannessen, T., 2017b. Dissolved inorganic carbon and total alkalinity at the Sudanese coastal Red Sea, 2009-2013, submitted to Regional Studies in Marine Sciences journal.

Beauverger,C., Brunet, C. Poisson, A. 1984a. MD 33/MEROU a bord du "MARION DUFRESNE" 16 juin au 4 juillet 1982,25 septcmbre au 4 octobre 1982. Les rapports des campagnes ala mcr, publication des T.A.A.F. No. 82-04, 181 pp.

Beauverger,C. 1984b. MD 33/MEROU a bord du "MARION DUFRESNE"]6 juin au 4 juillet 1982,25 septembre au 4 octobre 1982. Les rapports des campagnes a la mer, publication des T.A.A.F. No. 82-05,163 pp.

Behrenfeld, M. J., O'Malley, R., Siegel, D., McClain, C., Sarmiento, J., Feldman, G., Milligan, A., Falkowski, P., Letelier, R., Boss, E., 2006. Climate-driven trends in contemporary ocean productivity. Nature 444, 752–755.

Dickson, A.G., Millero, F.J., 1987. A comparison of the equilibrium constants for the dissociation of carbonic acid in seawater media. Deep-Sea Research 34, 1733–1743

Dickson, A. G., Sabine, C. L., Christian, J. R., 2007. Guide to best practices for ocean CO_2 measurements, p. 191. PICES Special Publication 3.

IMR, 2012. Environmental Baseline Study for Mersa El-Sheikh Ibrahim, conducted by Institute of Marine Research (IMR) in coloration with Faculty of Marine Sciences and Fishers (FMSF) at Red Sea University (RSU), Port Sudan, Sudan.

Johnson, K. M., Wills, K. D., Butler, D. B., Johnson, W. K., and Wong, C. S., 1993. Coulometric total carbon dioxide analysis for marine studies, Mar. Chem., 44, 167–187. 1993.

Key, R.M., Olsen, A., van Heuven, S., Lauvset, S. K., Velo, A., Lin, X., Schirnick, C., Kozyr, A., Tanhua, T., Hoppema, M., Jutterström, S., Steinfeldt, R., Jeansson, E., Ishii, M., Pérez, F. F., and Suzuki, T., 2015. Global Ocean Data Analysis Project, Version 2 (GLODAPv2), ORNL/CDIAC-162, NDP-P093. Carbon Dioxide Information Analysis Center, Oak Ridge National Laboratory, US Department of Energy, Oak Ridge, Tennessee. doi:10.3334/CDIAC/OTG.NDP093_GLODAPv2.

Körtzinger, A., 1999. Determination of carbon dioxide partial pressure (pCO_2), In: Methods of Seawater Analysis (eds.: K. Grasshoff, K. Kremling, M. Ehrhardt), Wiley-VCH, pp149-158.

Lefèvre, N., Taylor, A., 2002. Estimating pCO2 from sea surface temperatures in the Atlantic gyres, Deep Sea Res., Part I, 49, 539 – 554.

Le Quéré, C., Andrew, R. M., Canadell, J. G., Sitch, S., Korsbakken, J. I., Peters, G. P., Manning, A. C., Boden, T. A., Tans, P. P., Houghton, R. A., Keeling, R. F., Alin, S., Andrews, O. D., Anthoni, P., Barbero, L., Bopp, L., Chevallier, F., Chini, L.P., Ciais. P., Currie, K., Delire, C., Doney, S. C., Friedlingstein, P., Gkritzalis, T., Harris, I., Hauck, J., Haverd, V., Hoppema, M., Klein Goldewijk, K., Jain, A.K., Kato, E., Körtzinger, A., Landschützer, P., Lefèvre, N., Lenton, A., Lienert, S., Lombardozzi, D., Melton, J. R., Metzl, N., Millero, F., Monteiro, P.M.S., Munro, D.R., Nabel, J. E. M. N., Nakaoka, S.-i., O'Brien, K, Olsen, A., Omar, A. M., Ono, T., Pierrot, D., Poulter, B., Rödenbeck, C., Salisbury, J.E., Schuster, U., Schwinger, J., Séférian, R., Skjelvan, I., Stocker, B. D., Sutton, A.J., Takahashi, T., Tian, H., Tilbrook, B., van der Laan-Luijks, I. T., van der Werf, G.R., Viovy, N., Walker, A. P., Wiltshire, A.J., Zaehle, **S.,** 2016. Global carbon budget 2016, Earth Syst. Sci. Data, 8, 605–649,

Mehrbach, C. Culberson, C. H. Hawley, J. E., Pytkowicz, R. M., 1973. Measurement of the apparent dissociation constants of carbonic acid in seawater at atmospheric pressure. Limnology and Oceanography 18, 897-907.

Metzl, N., MooreIII, B., Papaud, A., Poisson, A., 1989. Transport and carbon exchange in Red Sea inverse methodology, Global Biogeochemical Cycle, Vol. 3, No. 1, pages 1-26.

Metzl, N., Poisson, A. Louanchi, F., Brunet, C., Schauer, B., 1995. Spatio-temporal distributions of air-sea fluxes of CO2 in the Indian and Antarctic Oceans: a first step. Tellus, 47B, 56-69.

Metzl, N. 2008. Sea Surface and Atmospheric fCO2 data in the Mediterranian Sea, Red Sea and Indian Ocean during the R/V Marion-Dufresne Minerve-40 cruise from Marseille (France) to La Reunion, Oct. 18 - Nov. 1, 1999.

Nightingale, P. D., Malin, G., Law, C.S., Watson, A. J., Liss, P. S., Liddicoat, M.I., Boutin, J., R. C. Upstill-Goddard, R. C., 2000. In-situ evaluation of air-sea gas exchange parameterizations using novel conservative and volatile tracers, Global Biogeochem. Cycles, 14, 373-387.

Olsen, A., Key, R. M., van Heuven, S., Lauvset, S. K., Velo, A., Lin, X., Schirnick, C., Kozyr, A., Tanhua, T., Hoppema, M., Jutterström, S., Steinfeldt, R., Jeansson, E., Ishii, M., Pérez, F. F., and Suzuki, T., 2016. The Global Ocean Data Analysis Project version 2 (GLODAPv2) – an internally consistent data product for the world ocean, Earth Syst. Sci. Data, 8, 297-323, https://doi.org/10.5194/essd-8-297-2016.

Omstedt, A., Gustafsson, E., and Wesslander, K., 2009. Modelling the uptake and release of carbon dioxide in the Baltic Sea surface water, Cont. Shelf Res., 29, 870–885.

Pierrot, D. E. L., Wallace, D. W. R., 2006. MS Excel Program Developed for CO2 System Calculations. ORNL/CDIAC-105a. Carbon Dioxide Information Analysis Center, Oak Ridge National Laboratory, U.S. Department of Energy, Oak Ridge, Tennessee. doi: 10.3334/CDIAC/otg.CO2SYS_XLS_CDIAC105a.

Raitsos, D. E., Hoteit, I., Prihartato, P. K., Chronis, T., Triantafyllou, G., Abualnaja, Y., 2011a. Abrupt warming of the Red Sea, Geophys. Res. Lett., 38, L14601, doi: 10.1029/2011GL047984.

Raitsos, D. E., Lavender, S. J., Maravelias, C. D., Haralabous, J., McQuatters-Gollop, A., Edwards, M. Reid, P. C., 2011b. Macroscale factors affecting diatom abundance: A synergistic use of Continuous Plankton Recorder and satellite remote sensing data, Int. J. Remote Sens., 32, 2081–2094, doi:10.1080/01431161003645832.

Raitsos, D. E., Pradhan, Y., Brewin, R. J. W., Stenchikov, G., Hoteit, I., 2013. Remote Sensing the Phytoplankton Seasonal Succession of the Red Sea. PLoS ONE 8(6): e64909. doi:10.1371/journal.pone.0064909.

Sweeney, C., Gloor, E., Jacobson, A. R., Key, R. M., McKinley, G., Sarmiento, J. L., and Wanninkhof, R., 2007. Constraining global air-sea gas exchange for CO2 with recent bomb C-14 measurements, Global Biogeochem. Cy., 21, GB2015, doi:10.1029/2006gb002784.

Souvermezoglou, T., Metzl, N., Poisson, A., 1989. Red Sea budgets of salinity, nutrients and carbon calculated in the Strait of Bab Al Mandab during summer and winter seasons, Journal of Marine Research, 47,441-456.

Taillandier, V., D'Ortenzio, F., Antoine, D., 2012. Carbon fluxes in the mixed layer of the Mediterranean Sea in the 1980s and the 2000s. Deep Sea Res. I 65, 73–84.

Takahashi, T., Olafsson, J., Goddard, J., Chipman, D.W., Sutherland, S.C., 1993. Seasonal variation of CO2 and nutrients in the high-latitude surface oceans: A comparative study. Glob. Biogeochem. Cycles 7, 843–878.

Takahashi, T., Feely, R.A., Weiss, R.F., Wanninkhof, R.H., Chipman, D.W., Sutherland, S.C., Takahashi, T.T., 2002. Global sea–air CO2 flux based on climatological surface ocean pCO_2, and seasonal biological and temperature effects. Deep-Sea Research II 49 (9–10), 1601–1622.

Wanninkhof, R., Olsen, A., Trin˜anes, J., 2007. Air–sea CO2 fluxes in the Caribbean Sea from 2002–2004. Journal of Marine Systems 66 (1–4), 272–284.

Weiss, R. F., 1974. Carbon dioxide in water and sea water: the solubility of a non -ideal gas, Mar. Chem., 2:203-215.

Weiss R. F., Broecker, W. S., Craig, H. B., Spencer., D. W., 1983. Geosecs Indian Ocean Expedition, 5. Hyd. data. Nat. Sc. Fond., U.S. Government Print. Off.

Yao, F. C., Hoteit, I., Pratt, L. J., Bower, A. S., Zhai, P., Kohl , A., Gopalakrishnan, G., 2014. Seasonal overturning circulation in the Red Sea: 1. Model validation and summer circulation. Journal of Geophysical Research-Oceans. 119:2238-2262.

Yilmaz A., De Lange G., Dupont S., Fine M., Fowler S.W., Gattuso J.P., Gazeau F., Gehlen M., Goyet C., Jeffree R., Montagna P., Rees A.P., Reynaud S., Rodolfo-Metalpa R., Ziveri P. and F. 2008. Briand Impacts of acidification on biological, chemical and physical systems in the Mediterranean and Black Seas Menton, 1 – 4 October 2008 I - EXECUTIVE SUMMARY OF CIESM WORKSHOP 36.

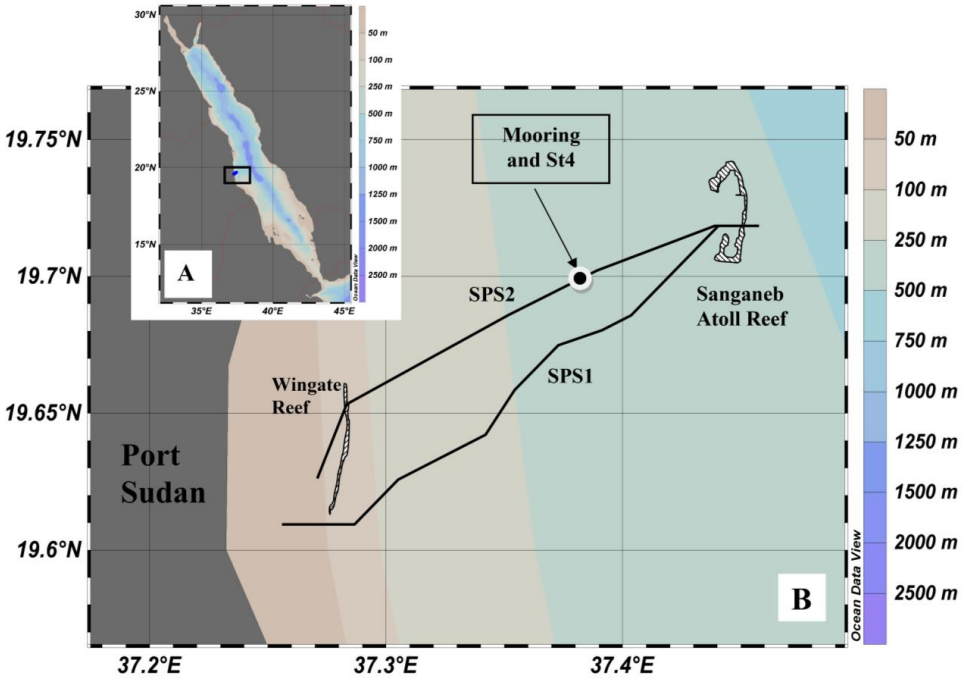

Fig.1: The mooring location between Port Sudan and Sanganeb atoll reef. The lines SPS1 and SPS2 indicate two time series transects described in Ali et al. (2017a; 2017b) and used in the current work. Note that the mooring position is the same as that of station 4 in the time series transect SPS2.

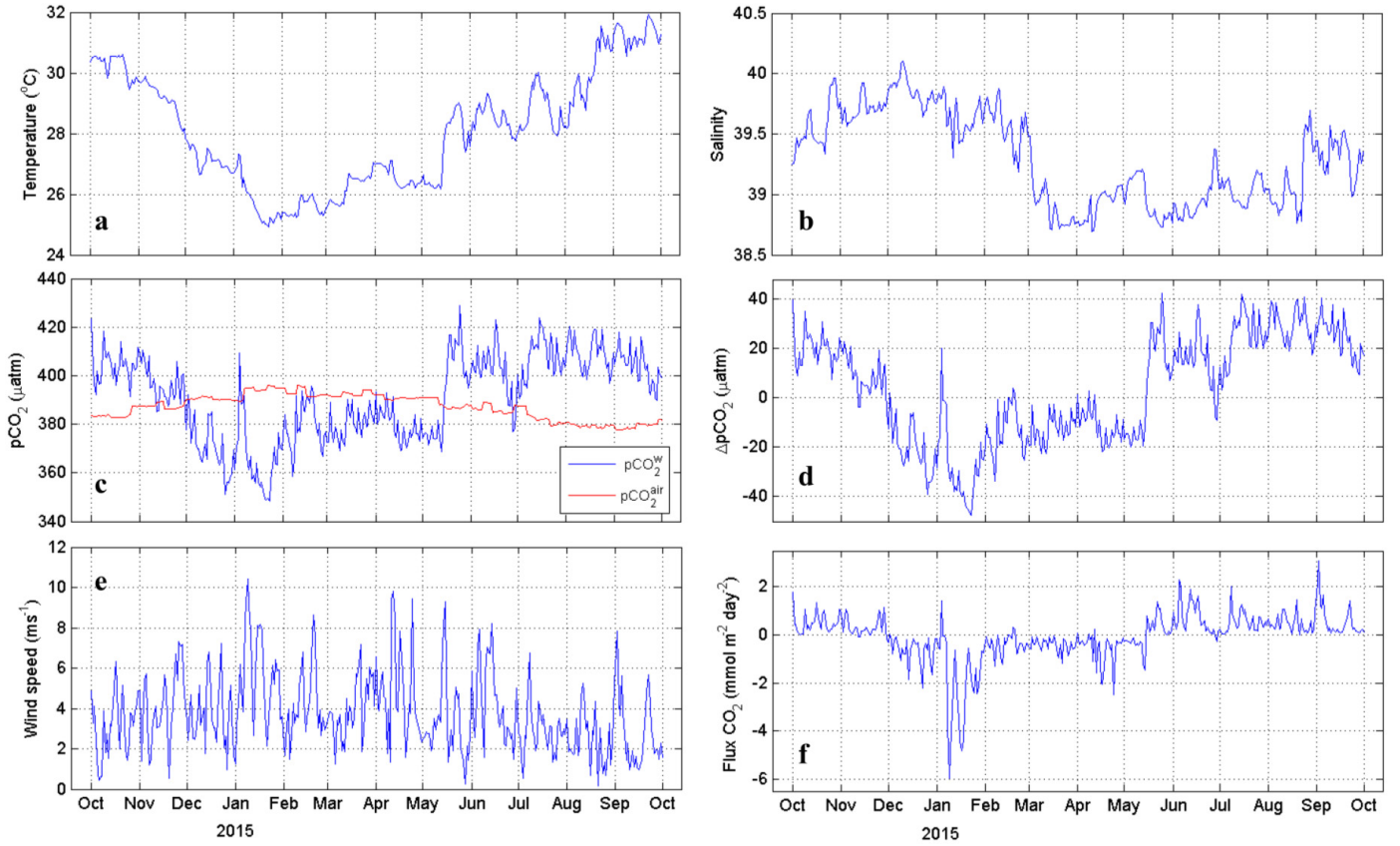

Fig. 2: Daily average of (a) temperature [°C], (b) salinity, (c) pCO_2^{air} and pCO_2^{w} [µatm], (d) ΔpCO_2 [µatm], (f) wind speed [m s^{-1}], and (g) CO_2 fluxes [mmol CO_2 m^{-2} day^{-1}].

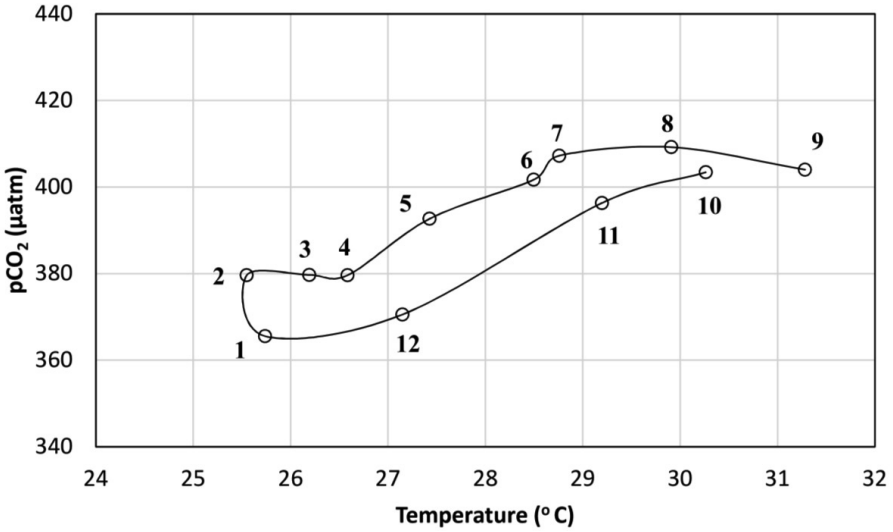

Fig. 3: Monthly averaged pCO_2^w [µatm] as a function of temperature [°C]. The black line indicates the annual cycles of the $pCO_2^w - SST$ changes. The number represent the month of sampling.

Fig. 4: The seasonal cycle of computed DIC (DIC_{Reg}) calculated based on multivariate regression coefficients of the SST-SSS-DIC relationship from Ali et al. (2017b).

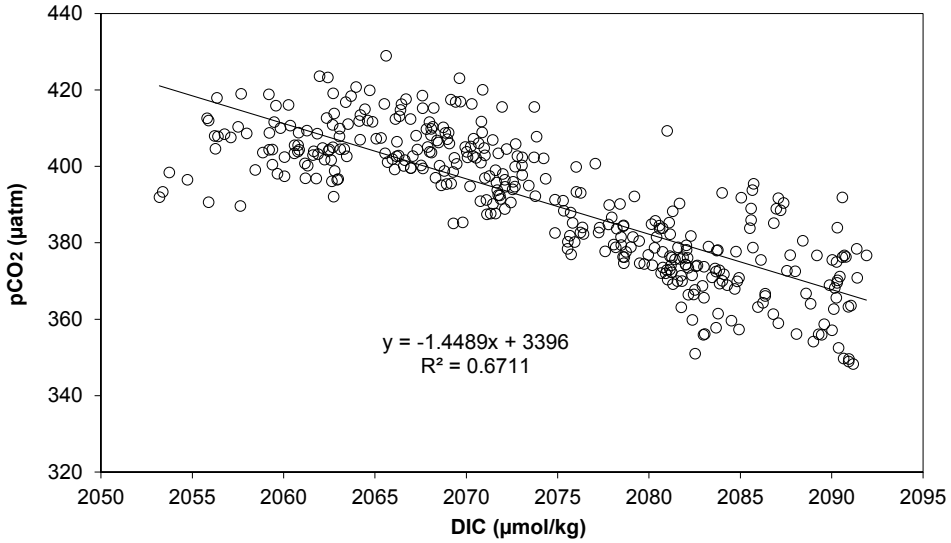

Fig.5 The relationship between pCO_2^w and DIC_{Reg}

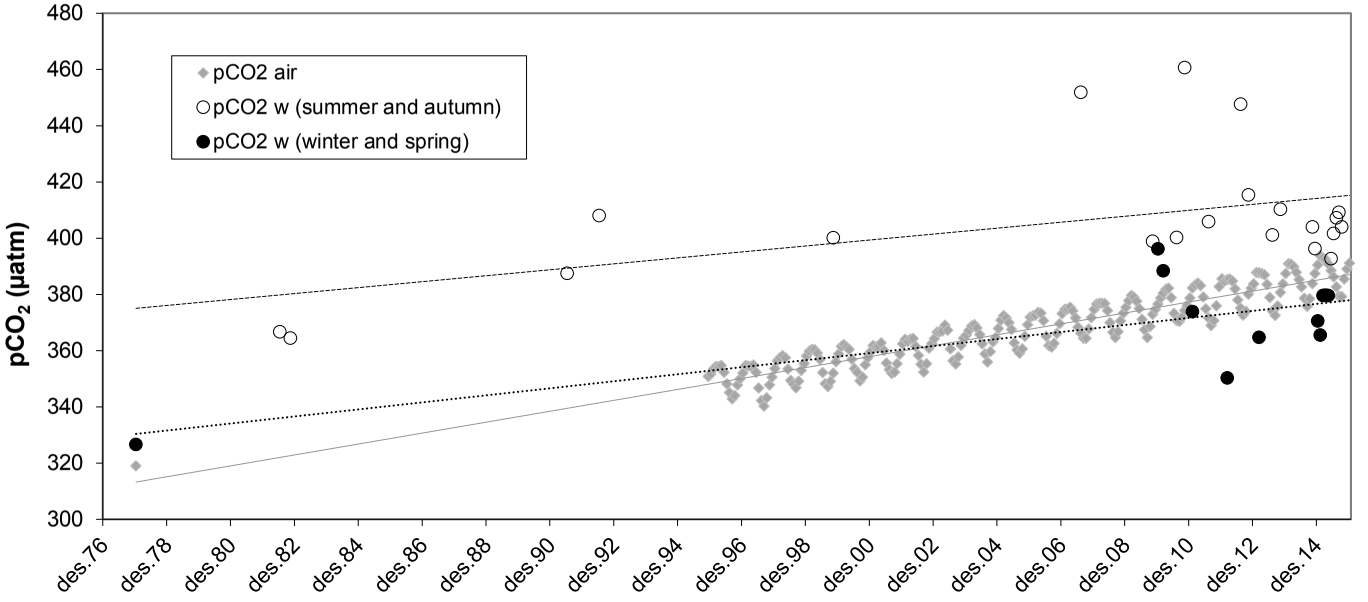

Fig. 6: Monthly average of atmospheric pCO_2 data from Sede Boker station and oceanic pCO_2 data from GEOSECS 1977 (Weiss et al., 1983), MEROU 1982 (I&II) (Beauverger et al., 1984), MINERVE 1991; 1992; 1999 (Metzl et al. 1995; 2008), Sanganeb 2007 (SPS1) (Ali, 2008), Sanganeb 2009-2013 (SPS2) (Ali et al., 2017b), and the mooring (current work). Trend lines are shown for pCO_2^w during summer and autumn (dashed line), pCO_2^w during winter and spring (dotted line), and atmospheric pCO$_2$ (grey solid line).